A Global Semianalytic Model of the First Stars and Galaxies Including Dark Matter Halo Merger Histories

Colton R. Feathers [ORCID], Mihir Kulkarni [ORCID], Eli Visbal [ORCID], and Ryan Hazlett [ORCID]
University of Toledo, Department of Physics and Astronomy and Ritter Astrophysical Research Center, 2801 W. Bancroft Street, Toledo, OH 43606, USA;
colton.feathers@rockets.utoledo.edu, mihir.kulkarni@utoledo.edu, elijah.visbal@utoledo.edu, ryan.hazlett@rockets.utoledo.edu

Abstract

We present a new self-consistent semianalytic model of the first stars and galaxies to explore the high-redshift ($z \gtrsim 15$) Population III (PopIII) and metal-enriched star formation histories. Our model includes the detailed merger history of dark matter halos generated with Monte Carlo merger trees. We calibrate the minimum halo mass for PopIII star formation from recent hydrodynamical cosmological simulations that simultaneously include the baryon–dark matter streaming velocity, Lyman–Werner (LW) feedback, and molecular hydrogen self-shielding. We find an overall increase in the resulting star formation rate density (SFRD) compared to calibrations based on previous simulations (e.g., the PopIII SFRD is over an order of magnitude higher at $z = 35-15$). We evaluate the effect of the halo-to-halo scatter in this critical mass and find that it increases the PopIII stellar mass density by a factor ~ 1.5 at $z \gtrsim 15$. Additionally, we assess the impact of various semianalytic/analytic prescriptions for halo assembly and star formation previously adopted in the literature. For example, we find that models assuming smooth halo growth computed via abundance matching predict SFRDs similar to the merger tree model for our fiducial model parameters, but that they may underestimate the PopIII SFRD in cases of strong LW feedback. Finally, we simulate subvolumes of the Universe with our model both to quantify the reduction in total star formation in numerical simulations due to a lack of density fluctuations on spatial scales larger than the simulation box, and to determine spatial fluctuations in SFRD due to the diversity in halo abundances and merger histories.

1. Introduction

Theoretical calculations based on the standard model of cosmology predict that the first stars began illuminating the Universe within the first ~ 100 Myr that followed the Big Bang. Simulations indicate these stars, categorized as Population III (PopIII) stars, formed from primordial metal-free gas within dark matter (DM) "minihalos" ($M_{\rm vir} = 10^5 - 10^6 \ M_\odot$), with much higher masses ($M_* = 10$–$1000 \ M_\odot$) than metal-enriched stars (for a recent review, see Klessen & Glover 2023). Thus, the first PopIII stars likely had stellar lifetimes of only a few megayears (Schaerer 2002). Following their short lives, they injected metal-enriched material into their surroundings via supernova (SN) winds, resulting in the formation of Population II (PopII) stars (see, e.g., Smith et al. 2015) and ultimately the first galaxies.

While there are currently no confirmed detections of PopIII stars, a variety of upcoming observations have the potential to constrain their abundance and properties (e.g., the PopIII initial mass function (IMF)). For example, the recently launched James Webb Space Telescope (JWST) may observe pair-instability SNe (Whalen et al. 2013; Hartwig et al. 2018a) from PopIII stars with initial masses ~ 140–$250 \ M_\odot$. If large clusters of PopIII stars form in so-called PopIII galaxies (e.g., due to inefficient mixing of metals), they may be directly observable with JWST (Visbal et al. 2017; Kulkarni et al. 2019; Sarmento et al. 2019; Vikaeus et al. 2022). We note that large PopIII starbursts detectable with JWST have recently been predicted

to occur in alternative DM scenarios that suppress small-scale structure, such as "fuzzy DM" (e.g., Hu et al. 2000; Hui et al. 2017; Ferreira 2021; Kulkarni et al. 2022). While PopIII stars currently remain elusive, JWST has already observed metal-enriched galaxies out to very high redshifts (e.g., Naidu et al. 2022; Finkelstein et al. 2023; Labbé et al. 2023). The properties of low-mass galaxies may even depend on the characteristics of PopIII stars due to the hierarchical nature of structure formation in the Lambda cold dark matter (ΛCDM) model (e.g., Abe et al. 2021).

Another promising route to constrain the properties of the first stars and galaxies is to measure their impact on the thermal and ionization properties of the intergalactic medium. For example, the optical depth due to electron scattering of the cosmic microwave background has been used to put upper limits on the efficiency of PopIII star formation (e.g., Haiman & Holder 2003; Shull & Venkatesan 2008; Ahn et al. 2012; Visbal et al. 2015a; Miranda et al. 2017). Additionally, the cosmological 21 cm signal is sensitive to the properties of early star formation. This is true both for global experiments such as EDGES (Bowman et al. 2018) and LEDA (Price et al. 2018), as well as those aiming to measure 3D spatial fluctuations, such as HERA (DeBoer et al. 2017) and the Square Kilometre Array (Mellema et al. 2013). Additional observational probes of PopIII stars include gamma-ray bursts (Bromm & Loeb 2007; Burlon et al. 2016; Kinugawa et al. 2019), line-intensity mapping of the 1640 Å He II recombination line (Visbal et al. 2015b; Parsons et al. 2022), and studying extremely metal-poor stars in the local Universe that could have been formed from the SN ejecta of PopIII stars ("stellar archeology;" e.g., Frebel & Norris 2015; Hartwig et al. 2015, 2018b; Magg et al. 2018).

The measurements described above require accurate theoretical models of early star and galaxy formation both to suggest

optimal observing strategies and interpret the results. Previous modeling efforts have taken many forms, from large-scale cosmological hydrodynamic simulations (e.g., Xu et al. 2013; Jaacks et al. 2018) to analytic calculations for quick predictions of global properties (e.g Haiman & Bryan 2006; Wyithe & Cen 2007; Trenti & Stiavelli 2009; Visbal et al. 2015a; Furlanetto & Mirocha 2022). While hydrodynamical cosmological simulations, such as the Renaissance Simulations (Xu et al. 2013, 2014; Ahn et al. 2015; O'Shea et al. 2015; Xu et al. 2016; Smith et al. 2018), include most of the physical processes relevant to early star formation, such as radiative, mechanical, and chemical feedback, they are very numerically expensive (e.g., $\sim 10^7$ CPU hours per realization in the case of Renaissance). While these simulations follow the physics with high fidelity, they still typically involve free parameters in subgrid prescriptions (e.g., the minimum metallicity for PopII star formation or the PopIII IMF), and are too costly to explore the parameter space in detail.

Semianalytic models of the first stars and galaxies represent an alternate approach that can be used to survey the uncertain parameter space rapidly, while accurately following the hierarchical assembly of DM structure (e.g., Trenti & Stiavelli 2009; Crosby et al. 2013; Valiante et al. 2016; Yung et al. 2019a). The DM "backbone" can be computed either through cosmological N-body simulations or analytic Monte Carlo (MC) methods based on the Extended Press–Schechter (EPS) formalism (Press & Schechter 1974; Bond et al. 1991). Star formation and astrophysical feedback is then implemented on top of this structure using analytic techniques, allowing for rapid simulation across cosmological volumes and large redshift ranges while still including most of the important physics (see Magg et al. 2018; Mebane et al. 2018; Visbal et al. 2018; Liu & Bromm 2020; Visbal et al. 2020, for examples).

In this paper, we present a new global high-redshift ($z \geqslant 15$) semianalytic model of the first stars and galaxies. The main new features of this model are that it includes complete DM halo merger histories (from MC methods) and is calibrated to state-of-the-art hydrodynamical cosmological simulations of the critical halo mass for PopIII star formation (Kulkarni et al. 2021). We utilize our model to make updated predictions of the high-redshift PopIII and metal-enriched star formation rate densities (SFRDs) and to test the impact of various physical effects/parameters (e.g., the baryon–DM streaming velocity). Given that our model incorporates a fully detailed DM halo merger history, we are also able to test the effect of approximations that have been adopted previously in literature to estimate the SFRD, such as smooth merger histories determined by halo abundance matching (e.g., Furlanetto et al. 2017; Mebane et al. 2018) and simple integrals of the halo mass function (e.g., Visbal et al. 2015a; Muñoz et al. 2022; Muñoz 2023). Finally, we use our model to simulate subregions of the Universe with different volumes, accounting for the Poisson fluctuations in the number of halos and their diverse merger histories. This allows us to estimate the impact of merger history on 3D spatial fluctuations of the PopIII and metal-enriched SFRDs relevant to future predictions of the cosmological 21 cm signal. It also allows us to show the impact on the SFRDs predicted by numerical simulations of finite box size that effectively ignore density fluctuations on spatial scales larger than the simulation box.

The remainder of this paper is structured as follows. In Section 2, we contextualize our new model by reviewing previous works in the literature. In Section 3, we discuss the details of our fiducial model and the physical processes included. The results of this work are divided into Sections 4, 5, and 6. Section 4 presents the main results of our fiducial model, and details the impact of various modeling fits and parameters on the global SFRD. Section 5 focuses on the impact of modeling choices for the DM halo evolution and the prescription for determining PopII star formation. Here we also check the accuracy of previous assumptions made in the literature regarding the effects of halo assembly on predicted SFRDs. In Section 6 we simulate finite, physically representative volumes of the Universe using our fiducial model. We compare our fiducial SFRDs with those previously published in the literature in Section 7. Finally, in Section 8 we summarize and discuss our results and explore future research. Unless otherwise stated, all distances are in comoving units. Throughout this work, we use a ΛCDM cosmology, consistent with Planck Collaboration et al. (2020) and with the parameters $\Omega_m = 0.32$, $\Omega_\Lambda = 0.68$, $\Omega_b = 0.049$, and $h = 0.67$.

2. Previous Works

In this section, we briefly review semianalytic works in the literature to provide context for our new model. The general approach in semianalytic modeling of galaxy evolution is to generate DM halo merger trees, either with MC methods or cosmological N-body simulations, and then apply analytic prescriptions for star formation and astrophysical feedback processes. This has been widely used to model galaxies at lower redshifts than those explored here (for a review see Somerville & Davé 2015). It has also been used to study high-redshift galaxies and reionization, but without including PopIII stars (e.g., Mutch et al. 2016; Poole et al. 2016; Yung et al. 2019b, 2020a, 2020b, 2021, 2022).

Described in detail in Section 3, we have adopted this framework to develop a global model of the first PopIII stars and early galaxies that includes a full DM halo merger history, incorporates self-consistent Lyman–Werner (LW) feedback (Haiman et al. 1997, 2000; Machacek et al. 2001; O'Shea & Norman 2008; Ahn et al. 2009), and is calibrated to recent hydrodynamical simulations. Most of the previous merger-tree–based semianalytic modeling of the first stars has been utilized to study the assembly of individual halos, rather than the global quantities on which we focus. This includes the formation of high-redshift supermassive black holes in rare high-mass halos (e.g., Valiante et al. 2016; Lupi et al. 2021; Trinca et al. 2022) as well as Milky Way–like halos to make predictions for stellar archeology (e.g., Ishiyama et al. 2016; de Bennassuti et al. 2017; Graziani et al. 2017; Griffen et al. 2018; Magg et al. 2018). We note that there have been previous global merger-tree–based models related to ours. In Magg et al. (2016), the PopIII SFRD was the focus; this is updated here with newly simulated critical halo masses for PopIII star formation (Kulkarni et al. 2021). More recently, Trinca et al. (2022) utilized EPS merger trees to study black hole and PopIII star formation, but this work focused on lower redshifts than what are explored here. We also note that toward the completion of this work, Ventura et al. (2023) and Trinca et al. (2023) presented similar global models of the first stars and galaxies. Their respective focuses were on the predicted 21 cm signal and UV luminosity functions, whereas we utilize our model to explore the impact of various physical effects and modeling techniques on the PopIII and metal-enriched SFRDs.

Table 1
Parameters and Fiducial Values Adopted in Our Framework for Modeling the Global SFRD

Parameter	Description	Fiducial Value	Reference
$\sigma_{\rm vbc}$	Relative baryon–DM streaming velocity	30 km s^{-1}	Tseliakhovich & Hirata (2010)
$\eta_{\rm III}$	# of LW photons per PopIII baryon	65,000	Schaerer (2002)
$\eta_{\rm II}$	# of LW photons per PopII baryon	4000	Samui et al. (2007)
$M_{\rm H_2}$	Molecular hydrogen cooling mass	$M_{z20}(J_{\rm LW}, v_{\rm bc})\left(\frac{1+z}{21}\right)^{\alpha(J_{\rm LW}, v_{\rm bc})}$	Kulkarni et al. (2021)
$M_{\rm a}$	Atomic hydrogen cooling mass	$5.4 \times 10^7 M_\odot \left(\frac{1+z}{11}\right)^{-1.5}$	Visbal et al. (2020)
$M_{\rm III,new}$	PopIII formation mass	$200\ M_\odot$	Skinner & Wise (2020)
$t_{\rm delay}$	Delay time before PopII star formation	10 Myr	Jeon et al. (2014)
$f_{\rm II}$	Enriched star formation efficiency (SFE)	0.0025	See Section 3.2.3 in main text
$\eta_{\rm SN}$	SN ejection efficiency	$5.23 \times \left(\frac{v_{\rm esc}}{14.46\ {\rm km\ s^{-1}}}\right)^{-2}$	Sassano et al. (2021)

An additional novel aspect of our work is that we use our model to understand the behavior of various subvolumes of the Universe as a step toward accurate modeling of the 3D spatial fluctuations of high-redshift star formation.

Several recent semianalytic works have included 3D spatial information from N-body simulations (in addition to merger trees) to model the effects of ionization feedback and "external" metal-enrichment between neighboring halos (e.g., Sarmento et al. 2019; Liu & Bromm 2020; Visbal et al. 2020; Hartwig et al. 2022). This is complementary to the work presented here. Although our fiducial model cannot properly include 3D feedback (since MC EPS methods are used to generate the merger trees), it has been found that 3D feedback does not have a significant impact on the SFRDs at $z \gtrsim 15$ (Visbal et al. 2020), which is when we have decided to stop our models presented below. With our semianalytic framework, we are able to rapidly explore much larger volumes than what is possible when N-body simulations are used.

In addition to these semianalytic methods, analytic works have been used to model the global abundances of the first stars and galaxies. These include what we refer to as "smooth accretion models" where halo growth histories are approximated using abundance matching of the halo mass function (Furlanetto et al. 2017; Mebane et al. 2018, 2020). A number of previous works have also estimated the SFRDs of PopIII and metal-enriched stars via analytic integration of the halo mass function (e.g., Visbal et al. 2015a; Muñoz et al. 2022; Muñoz 2023). We use our model below to test the impact that these approximations related to halo assembly have on the global star formation history.

We also note that our new model relates to large-scale seminumerical models which have been used to predict the high-redshift 21 cm signal (Mesinger et al. 2011; McQuinn & O'Leary 2012; Visbal et al. 2012; Fialkov et al. 2013; Fialkov & Barkana 2014; Kaur et al. 2022; Magg et al. 2022). These models simulate vast cosmological volumes (e.g., boxes ∼1 Gpc across) with individual resolution elements that are a few megaparsecs across. Within these volume elements, the local SFRD is typically computed with integrals of the halo mass function (e.g., Jaacks et al. 2018), though recent work has been calibrated with merger-tree–based semianalytic models (Magg et al. 2022). Utilizing our model to simulate variations within individual subvolumes (as we present in Section 6) can lay the groundwork to improve future subgrid prescriptions within large-scale seminumerical models.

3. Fiducial Semianalytic Model

In this section, we introduce our fiducial semianalytic model whose purpose is to determine the evolution of the global SFRD self-consistently (along with other aspects of early star formation such as the scatter in the SFRDs within subvolumes of the Universe) given some input DM halo model, star formation prescription, and parameter values. We note that the efficiency of this framework allows each realization to be completed in ∼75 minutes on a single CPU. Our fiducial modeling parameters are summarized in Table 1 and described in more detail below.

3.1. DM Halo Merger History

Our model uses MC merger trees based on EPS formalism (Press & Schechter 1974; Bond et al. 1991) to model DM halo growth. We generate merger trees following the prescription in Lacey & Cole (1993), which assumes binary mergers of DM halos at each redshift step, separated by Δz. For a given final halo mass and redshift, the merger history is modeled by iteratively stepping back through time, determining the first progenitor halo mass via the EPS mass-weighted progenitor function, and setting the second progenitor halo mass such that the sum of the two progenitors is equal to the merged descendent halo mass. This is done for each halo by solving Equation (5) of Visbal et al. (2014) for σ_{M_1}, the rms density fluctuation on a scale corresponding to mass M_1,

$$\sigma_{M_1} = \sqrt{\sigma_{M_0}^2 + \frac{1}{2}\left(\frac{\delta_{\rm crit}}{{\rm erf}^{-1}(x)}\right)^2 \left(\frac{1}{D(z+\Delta z)} - \frac{1}{D(z)}\right)^2}. \quad (1)$$

Here, σ_{M_0} is the rms density fluctuation for the scale corresponding to the present halo mass, $\delta_{\rm crit} = 1.686$ is the critical overdensity in linear perturbation theory, $D(z)$ is the linear growth factor, and x is a randomly drawn value between 0 and 1. From σ_{M_1} we determine the progenitor halo mass, M_1, and the merging halo progenitor mass, $M_2 = M_0 - M_1$. This process is repeated at each step back through cosmic time until a halo falls below the resolution halo mass, $M_{\rm res}$, after which no further progenitors are modeled. To account for any statistically rare merger histories, we generate multiple merger trees for each halo mass bin whose masses are set at the end of the simulation, $z = 15$.

In our fiducial model we use 36 logarithmically spaced mass bins from $10^{5.6}$ to $10^{9.1}\ M_\odot$, finding this mass range to be sufficiently converged for estimating the global SFRD between

$z = 15$ and 35. These precise mass values have little physical motivation; we simply find that adding halo mass bins above $10^{9.1} \, M_\odot$ only affects the results at the earliest redshifts ($z \gtrsim 42$), and that the critical mass for PopIII star formation is higher than $10^{5.6} \, M_\odot$ at $z = 15$ in all reported runs, indicating lower mass bins would not contribute to the resulting SFRDs. We also varied the number of halo mass bins and found that our fiducial number of bins yields SFRD values that converge to within 10% on average between $z = 15$ and 35. Within each mass bin we generate 10 merger trees each initialized at $z = 15$, finding this number of trees to be the most reasonable trade-off between the required computation time and the statistical noise in our resulting SFRDs. We adopt a resolution halo mass of $M_{\rm res} = 5 \times 10^4 \, M_\odot$ for our merger trees, a threshold well below typical values of $M_{\rm crit}$ so that no early star formation is missed. We run our models from $z = 60$ to 15, with redshift steps of $\Delta z = 0.05$. Overall, we find the results of our work to be sufficiently converged for predicting the globally averaged SFRD over the redshift range $z = 15$–35.

3.2. Star Formation

Here we discuss the methods used to determine the formation of both PopIII and PopII stellar mass within merger-tree halos. Note that we do not track individual stars in our model, and so any PopII and PopIII stellar masses discussed are total mass values. We focus mainly on the high-redshift transition from PopIII to PopII and leave any analysis of the transition from PopII to Population I for future work.

3.2.1. Critical Mass and PopIII Star Formation

We use a simple "instantaneous" prescription for PopIII star formation in our fiducial model. A given halo without previous star formation will undergo a single episode of pristine star formation, creating a constant stellar mass of $M_{\rm III,new} = 200 \, M_\odot$ immediately after it surpasses the critical mass for star formation, $M_{\rm crit}$. This is roughly consistent with the average PopIII stellar mass found within halos by Skinner & Wise (2020; see their Figure 8), and approximately corresponds to a constant PopIII star formation efficiency (SFE) of $f_{\rm III} = 0.0001$ for a halo of mass $10^{6.1} \, M_\odot$.

The critical mass is a global threshold for PopIII star formation, determined at each time step by finding the smaller of the atomic and molecular hydrogen cooling halo masses, i.e.,

$$M_{\rm crit} = \min(M_{\rm a}, M_{\rm H_2}). \tag{2}$$

Since the gas within early DM halos is pristine, molecular hydrogen (H$_2$) is initially the most efficient gas coolant. As star formation proceeds, the resulting radiative feedback dissociates H$_2$ molecules, effectively raising the halo virial temperature and therefore $M_{\rm H_2}$. For halos with virial temperatures $T_{\rm vir} \gtrsim 10^4$ K, atomic hydrogen cooling becomes the more efficient mode of halo cooling, and so we adopt our atomic cooling mass from Visbal et al. (2020),

$$M_{\rm a} = 5.4 \times 10^7 \, M_\odot \left(\frac{1+z}{11}\right)^{-1.5}. \tag{3}$$

This mass is based on the threshold found in hydrodynamic cosmological simulations, with precise values from Fernandez et al. (2014). The H$_2$ cooling mass used in our fiducial model is adopted from the hydrodynamical simulations of Kulkarni et al.

(2021), which are the first (along with Schauer et al. 2021) to include a dependency on both the relative baryon–DM streaming velocity, $v_{\rm bc}$, and the LW radiation background intensity, $J_{\rm LW}$ (also see Nebrin et al. 2023). They also consider an improved treatment of H$_2$ self-shielding, ultimately leading to an analytic fitting function that is well calibrated to the hydrodyamical simulations,

$$M_{\rm H_2} = M_{\rm z20}(J_{\rm LW}, v_{\rm bc}) \left(\frac{1+z}{21}\right)^{\alpha(J_{\rm LW}, v_{\rm bc})}. \tag{4}$$

Here, the critical mass at $z = 20$, $M_{\rm z20}$, and the power-law index, α, are both functions of the LW background intensity and baryon–DM streaming velocity (see Kulkarni et al. 2021 for the best-fit values of these parameters to the simulations). At each time step, our semianalytic model determines which halos have masses above $M_{\rm crit}$ and forms $M_{\rm III,new}$ within each.

In Section 4.1, we compare the results of our fiducial model, with $M_{\rm H_2}$ determined by Equation (4), to a previous model of $M_{\rm H_2}$ based on the simulations of Machacek et al. (2001; also see Greif et al. 2011; Stacy et al. 2011; Fialkov et al. 2012). This molecular mass fit, or variations thereof, has commonly been used in simulations of early star formation throughout the literature. Here we implement the form used in Visbal et al. (2014) which includes a dependence on the redshift,

$$M_{\rm H_2} = 2.5 \times 10^5 \left(\frac{1+z}{26}\right)^{-1.5} (1 + 6.96(4\pi J_{\rm LW})^{0.47}). \tag{5}$$

The key difference between this and our fiducial equation for $M_{\rm H_2}$ is that the fit presented in Kulkarni et al. (2021) includes the effects of H$_2$ self-shielding and a stronger relative baryon–DM streaming velocity dependence. Fitting functions based on previous simulations, including those of Machacek et al. (2001), either do not include $v_{\rm bc}$, or assumed that the LW intensity and $v_{\rm bc}$ were independent modeling processes and their effects on $M_{\rm crit}$ were multiplicative (Fialkov et al. 2012). As shown by Kulkarni et al. (2021), their effects on $M_{\rm crit}$ are not multiplicative, hence our choice of this $M_{\rm H_2}$ fit for our fiducial model.

3.2.2. Delay Time for Enriched Star Formation

A key parameter of our semianalytic model is the delay time between the formation of PopIII and metal-enriched PopII stars, $t_{\rm delay}$. This delay period is a result of the radiative and SN feedback from the first stars which heats and ejects gas from within the hosting minihalos. Once the halo gas reservoir recollects and cools once more, the enriched material begins forming PopII stars (Chiaki et al. 2013; Jeon et al. 2014; Chiaki et al. 2017). We choose $t_{\rm delay} = 10$ Myr for our fiducial model, and explore the impact of different $t_{\rm delay}$ values on the resulting SFRDs in Section 4.4.

3.2.3. PopII Star Formation

We assume that once PopIII stars form in a halo and the delay time has elapsed, it begins forming metal-enriched PopII stars. For PopII star formation, we adopt the system of differential equations described in Furlanetto & Mirocha (2022) that simultaneously determines the gas and stellar masses of a given halo through a simplified "bathtub" model (e.g.,

Bouché et al. 2010; Davé et al. 2012; Dekel & Mandelker 2014),

$$\dot{M}_{*,\mathrm{II}} = \frac{f_{\mathrm{II}}}{t_{\mathrm{ff}}} M_{\mathrm{gas}}, \tag{6}$$

$$\dot{M}_{\mathrm{gas}} = \dot{M}_{\mathrm{acc}} - \dot{M}_{*,\mathrm{II}}(1 + \eta_{\mathrm{SN}}). \tag{7}$$

Here, $\dot{M}_{*,\mathrm{II}}$ is the halo PopII star formation rate (SFR), f_{II} is the PopII SFE per halo freefall time, t_{ff}, which we assume to be 10% of the Hubble time (i.e., $t_{\mathrm{ff}} = 0.1\ t_{\mathrm{H}}$), $\dot{M}_{\mathrm{gas}}$ represents the time derivative of the halo gas mass, $\dot{M}_{\mathrm{acc}}$ is the mass accretion rate of the halo, and η_{SN} is the SN ejection efficiency (described in more detail below). By analytically solving these differential equations at each time step, we obtain the gas and stellar masses of each halo, and determine the gas mass ejected through SNe by subtracting these two masses from the initial total baryonic mass of the halo. This prescription forms stars such that a fraction of the total halo gas mass, f_{II}, is converted into stellar mass over one halo freefall time, allowing isolated DM halos to continue forming PopII stars as long as there is gas within them.

While we note that there is large uncertainty in the SFE of unobserved low-mass galaxies at very high redshifts ($z \gtrsim 15$), we have aimed to select a realistic value for our fiducial choice of $f_{\mathrm{II}} = 0.0025$. When combined with the SN feedback prescription described below, we find that this choice of f_{II} leads to an SFRD consistent with Visbal et al. (2018), which was calibrated to observations of $z \sim 6$ UV galaxy luminosity functions (Bouwens et al. 2015). In a related upcoming study (R. Hazlett et al. 2024, in preparation), we have created a model of PopII star formation directly calibrated to the Renaissance simulations. We find that this calibration yields PopII SFRDs that agree to within a factor of two at $z \lesssim 32$ with those predicted in our fiducial model presented here.

At each time step, we determine the PopII and PopIII SFRs for each merger tree by dividing any new stellar mass formed by the length of the time step. We average the SFRs of all merger trees in each mass bin, and weight each average by the corresponding halo mass bin number density, n_i, as determined from the Sheth–Tormen halo mass function (Sheth & Tormen 1999) at the bin center, i.e.,

$$n_i = \int_{m_1}^{m_{\mathrm{u}}} \frac{dn}{dM} dM. \tag{8}$$

Here, dn/dM is the Sheth–Tormen halo mass function and n_i is the number density of halos at $z = 15$ in mass bin i, respectively bounded by upper and lower halo masses m_{u} and m_1. For the remainder of this paper, all DM halo mass bin number densities are the $z = 15$ values unless otherwise stated. The weighted averages of all mass bins are then summed to give the global PopII and PopIII SFRD values for that redshift step, i.e.,

$$\mathrm{SFRD}(z) = \sum_i n_i \langle \dot{M}_{*,\mathrm{tot}} \rangle_i. \tag{9}$$

Here, $\dot{M}_{*,\mathrm{tot}}$ is the total SFR of every halo at redshift z within a merger tree in mass bin i. We average the total SFRs of all merger trees in mass bin i to get $\langle \dot{M}_{*,\mathrm{tot}} \rangle_i$ which we then weight by n_i and sum across all mass bins.

3.3. Feedback Processes

Our semianalytical framework also includes various crucial feedback processes that impact the global SFRD evolution. In this subsection, we will discuss the auxiliary features and physical feedback processes of our fiducial model and how they affect early star formation.

3.3.1. LW Background Intensity

LW feedback must be considered in any semianalytic model of early star formation. As the first stars begin to shine and emit radiation, photons in the energy range $E_{\mathrm{LW}} = 11.2$–13.6 eV freely stream out up to a horizon of ~ 100 Mpc and into other DM halos, dissociating H_2 molecules within them (Haiman et al. 1997, 2000; Machacek et al. 2001; O'Shea & Norman 2008; Ahn et al. 2009). In our fiducial model, we self-consistently determine the LW background intensity at each time step in units of 10^{-21} erg s^{-1} cm^{-2} Hz^{-1} sr^{-1} using the J_{LW} calculation from Visbal et al. (2020),

$$J_{\mathrm{LW}}(z) = \frac{c(1+z)^3}{4\pi} \int_z^\infty \epsilon_{\mathrm{LW}}(z') \left| \frac{dt_{\mathrm{H}}}{dz'} \right| f_{\mathrm{LW}}(z', z) dz'. \tag{10}$$

Here, $\epsilon_{\mathrm{LW}}(z')$ is the mean LW emissivity, t_{H} is the Hubble time, and $f_{\mathrm{LW}}(z', z)$ is the attenuation of the LW flux from z' to z as LW photons redshift into Lyman series lines and are absorbed (Haiman et al. 1997). We approximate this LW attenuation using Equation (22) in Ahn et al. (2009), and determine $\epsilon_{\mathrm{LW}}(z')$ by summing the contributions of both stellar populations.

We assume the number of LW photons produced per stellar baryon to be $\eta_{\mathrm{III}} = 65{,}000$ for PopIII stars (Schaerer 2002), and $\eta_{\mathrm{II}} = 4000$ for metal-enriched stars (Samui et al. 2007; Incatasciato et al. 2023). We set these to be equal to the number of ionizing photons produced per stellar baryon for simplicity, and also note that our assumed value of η_{III} may be an overestimate, but we have found that the PopII SFRD quickly dominates the LW background in all runs, and varying η_{III} only changes the PopIII SFRD by a few percent. An increase in J_{LW} results in an increase in both M_{z20} and α in Equation (4), giving a larger M_{H_2} for Equation (2). Increased LW radiation intensity therefore results in an overall increase to the critical mass for PopIII star formation, suppressing further star formation.

In our model, we do not consider the effects of X-ray feedback on PopIII star formation. We note that Hegde & Furlanetto (2023) recently found that the X-ray background is not a dominant effect for PopIII star formation in minihalos at the redshifts considered in this work ($z > 15$; also see Ricotti & Ostriker 2004; Ricotti 2016).

3.3.2. Relative Baryon–DM Streaming Velocity

Another important parameter in modeling early star formation is the relative streaming velocity between baryons and DM (Tseliakhovich & Hirata 2010; Greif et al. 2011; Tseliakhovich et al. 2011; Stacy et al. 2012; Fialkov et al. 2013). At cosmic recombination, photons decoupled from the baryonic matter which was then free to interact gravitationally. DM density perturbations, however, could grow under the influence of gravity before this. As a result, we are left with a Maxwell–Boltzmann distribution of relative baryon–DM streaming velocities with an rms value of $\sigma_{\mathrm{vbc}} = 30$ km s^{-1} at

recombination, which decreases with redshift as $v_{bc}(z) = v_{bc,0}$ $((1+z)/1100)$. This relative motion is roughly constant over scales ∼3 Mpc, and is crucial for modeling early star formation because the DM halos are unable to capture and cool the high-speed gas streaming by them efficiently. An increase in streaming velocity leads to a decrease in the amount of gas bound to halos and delays halo gas cooling, thus leading to an overall increase in M_{crit}. The value of this velocity is commonly referred to in terms of σ_{vbc}, and while we explore the impact of various σ_{vbc} values below, we adopt a fiducial global streaming velocity of $v_{bc} = 1\sigma_{vbc} = 30$ km s^{-1}.

3.3.3. Feedback from SNe

A fraction of the gas mass within a given halo will be ejected by the star formation and SNe occurring at a given time step. The gas mass ejected by PopII SNe is determined by the SN ejection efficiency of the halo, η_{SN}. In this work, we follow a similar prescription for determining η_{SN} to the one presented in Sassano et al. (2021),

$$\eta_{SN} = \frac{2E_{SN}\,\epsilon_{SN}R_{SN}}{v_{esc}^2}, \tag{11}$$

where E_{SN} is the average energy per PopII SN, ϵ_{SN} is an efficiency parameter, R_{SN} is the rate of SNe per solar mass, and v_{esc} is the escape velocity of the halo, which we assume to be the halo circular velocity determined by Equation (25) of Barkana & Loeb (2001). We note that the circular and escape velocities at a halo's virial radius differ by a factor of $\sqrt{2}$, however the effect that SN ejection has on the global SFRD is comparatively low (i.e., removing all SN feedback results in a ∼30% increase to the $z = 15$ PopII SFRD), and since we do not assume a preferred radius for SN ejection from our DM halos, we adopt the circular velocity for simplicity. We adopt values of $E_{SN} = 10^{51}$ erg and $\epsilon_{SN} = 0.0016$ from Wise et al. (2012). R_{SN} is determined by dividing the SN energy per solar mass, $E_{SN,M_\odot}$, by E_{SN}. Adopting a value of $E_{SN,M_\odot} = 6.8 \times 10^{48}$ erg $M_\odot^{-1}$ (Wise et al. 2012) gives us $R_{SN} = 0.0068\ M_\odot^{-1}$. The numerator of Equation (11) can then be described in terms of velocity, and so we normalize this expression for a halo at $z = 20$ with a mass equal to the atomic cooling mass (Equation (3)). This gives us $\eta_{SN} = 5.23 \times (v_{esc}/14.46$ km s$^{-1})^{-2}$.

The ejected gas mass, M_{ej}, is determined at each time step by subtracting the final stellar and gas masses within the halo from its initial total baryonic mass. M_{ej} is then removed from the available halo gas mass until it is reintroduced for future star formation after one freefall time, which we have assumed to be 10% of the Hubble time at the moment of ejection.

4. Results. I. Fiducial Model

In this section we present the global SFRDs of our fiducial model. We illustrate the effects of a new critical mass model (Equation (4)) that more accurately considers the effects of LW feedback, v_{bc}, and H_2 self-shielding, as well as the impact of halo-to-halo scatter on M_{crit}. We also assess the impact that various physical processes and parameter value choices have on the results. Unless otherwise stated, all SFRD values plotted throughout this work have been smoothed postsimulation with a running average over $\Delta z = 1$. We also provide analytic fits

for a sample of the LW backgrounds that result from this research in Appendix.

4.1. Critical Mass Model

Figure 1 shows the SFRDs and corresponding critical masses resulting from both our fiducial model with M_{crit} based on the new simulations of Kulkarni et al. (2021), and those resulting from the Visbal et al. (2020) adaptation of the commonly used critical mass model consistent with the simulations of Machacek et al. (2001), Greif et al. (2011), and Stacy et al. (2012) in which the effects of H_2 self-shielding are not considered. This "no self-shielding" M_{crit} model stems from the work of Fialkov et al. (2012), which updated the critical mass threshold from Machacek et al. (2001) to include more sophisticated treatments for v_{bc} dependence (also see Equation (3) of Visbal et al. 2020 and the accompanying text for more information on including LW and v_{bc} dependences). However, since recent works have revised the critical mass threshold for PopIII star formation to include the effects of H_2 self-shielding (e.g., Kulkarni et al. 2021; Schauer et al. 2021; Nebrin et al. 2023), we refer to this earlier M_{crit} as the "no self-shielding" critical mass model for the remainder of this paper.

The left set of plots is for a global streaming velocity of $1\sigma_{vbc}$. Here we see that our fiducial critical mass is a factor of a few lower than the no self-shielding model throughout, falling to a factor ∼six times lower at $z \sim 15$. This lower M_{crit} leads to earlier star formation and an overall larger number of star-forming halos in the fiducial model. We thus find a PopIII SFRD that is over an order of magnitude higher than the no self-shielding PopIII SFRD throughout most of the redshifts shown. The fiducial PopII SFRD is also consistently higher than the one given by the no self-shielding M_{crit}, but this difference falls from an order of magnitude at $z = 35$ to a factor of two times the no self-shielding PopII SFRD at $z = 15$.

The right set of plots in Figure 1 show the results for no baryon–DM streaming. Here we see a somewhat smaller difference in the SFRDs. At $z = 35$, our fiducial model gives SFRD values that are factors of 30 and 8 times higher than the no self-shielding values for PopIII and PopII, respectively. The final PopII SFRD of the fiducial model is only 30% higher than the no self-shielding case, whereas the final PopIII SFRD is a factor ∼two higher. Here, the effects that cause the differences in the $1\sigma_{vbc}$ case are reduced because the critical masses fall within a factor of five to one another throughout, owing to the stronger v_{bc} dependence in the no self-shielding model.

4.2. Critical Mass Scatter

In our fiducial model we assume M_{crit} to be a global constant at each time step; we now consider the impact of scatter on $M_{crit}(z)$, which effectively gives each DM halo an individual critical mass threshold for PopIII star formation, $M_{crit,halo}$. To account for variations in halo mass assembly and geometry more accurately, Kulkarni et al. (2021) quantified this scatter in terms of J_{LW} and v_{bc}, which we may implement via,

$$\log_{10}(M_{crit,halo}) = \log_{10}(M_{crit}) + R. \tag{12}$$

Here, the value of R is determined for each DM halo after every halo freefall time by randomly drawing from a Gaussian distribution centered on zero and with a standard deviation of $\sigma = 0.15$. The M_{crit} scatter values reported in Figure 7 of Kulkarni et al. (2021) represent the difference between the 25th
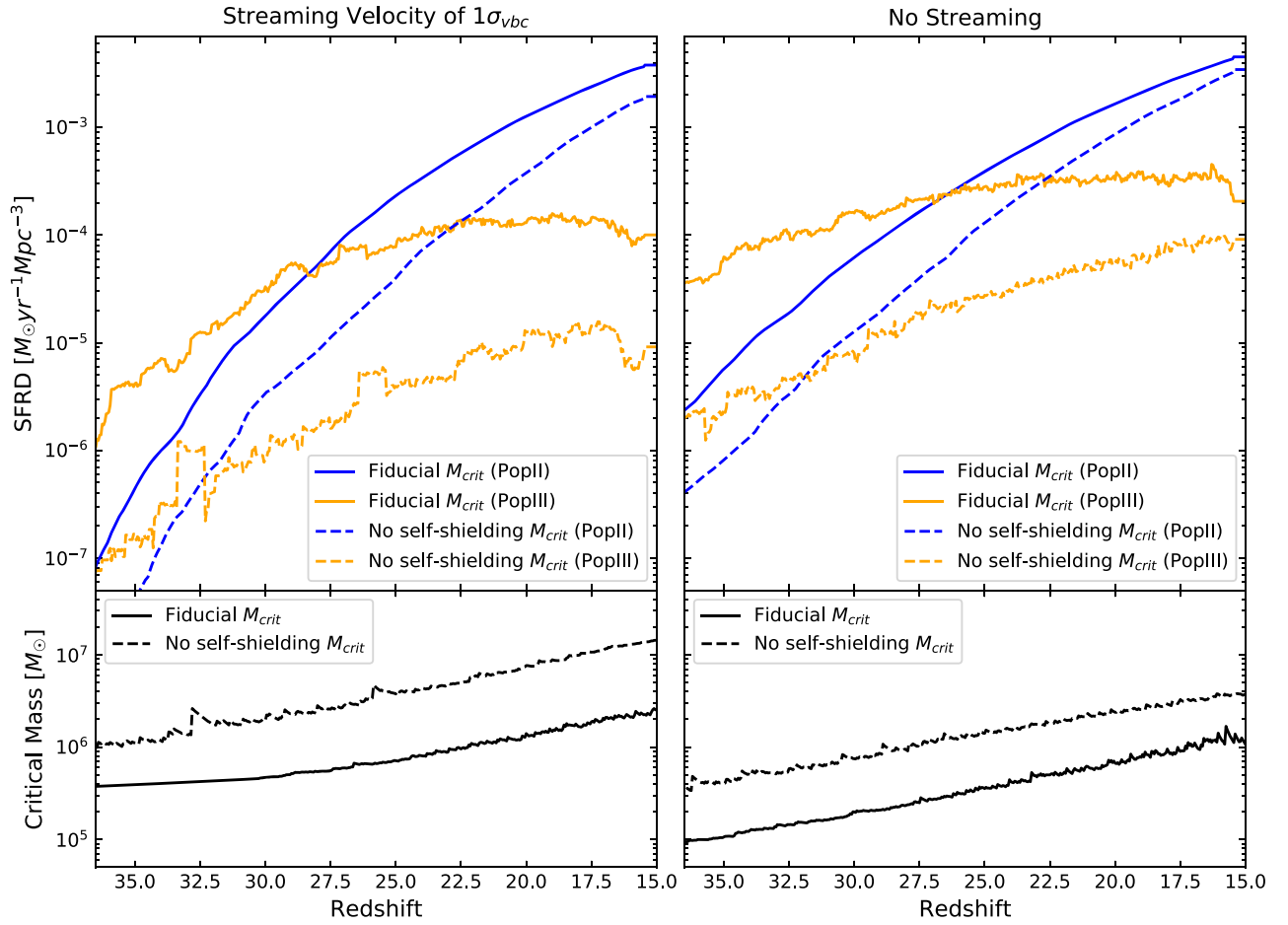
Figure 1. The impact of different critical mass calculation methods for realizations including (left column) and not including (right column) relative baryon–DM streaming. Top left: comparison of the PopII (blue) and PopIII (orange) SFRDs with different methods for determining $M_{\rm crit}$, including a global streaming velocity of $1\sigma = 30$ km s^{-1}. Our fiducial framework using the Kulkarni et al. (2021) $M_{\rm crit}$ model (solid) is compared to a realization using the critical mass model from Visbal et al. (2020), based on the simulations of Machacek et al. (2001; dashed). Top right: same as the top left, but for realizations with no global baryon–DM streaming (i.e., $v_{\rm bc} = 0$ km s^{-1}). Bottom left: the value of $M_{\rm crit}(z)$ for each method with a streaming velocity of $1\sigma_{\rm vbc}$. Bottom right: same as the bottom left but with no baryon–DM streaming.

and 75th percentiles of the critical masses, equivalent to 1.34σ. For a streaming velocity of $1\sigma_{\rm vbc}$, this value ranges from 0.15 to 0.3, and we adopt the value 0.2, roughly corresponding an LW background intensity of $J_{\rm LW} = 1 \times 10^{-21}$ erg s^{-1} cm^{-2} Hz^{-1} sr^{-1}. Although we self-consistently determine $J_{\rm LW}$ at each time step, its values at $z \lesssim 30$ are comparable to unity, and so we conservatively adopt $\sigma = 0.15$ ($\simeq 0.2/1.34$) for the standard deviation of our distribution. (for more information, see Figure 7 of Kulkarni et al. 2021).

We illustrate the impact of this relative scatter on $M_{\rm crit}$ in Figure 2. The solid lines in the top panel show the stellar mass densities (SMDs) for both PopII and PopIII as determined by our fiducial model. The SMDs of 10 simulations including $M_{\rm crit}$ scatter are shown in light gray for each stellar population, and the averages of these 10 SMDs are represented by the corresponding dashed lines. We choose to show the SMDs in Figure 2 rather than the SFRDs to show more clearly the impact that $M_{\rm crit}$ scatter has on the star formation resulting from our semianalytic model.

We see from the bottom panel of Figure 2 that introducing $M_{\rm crit}$ scatter increases the PopIII SMD by a factor ~two at early times ($z \gtrsim 30$). Below $z \sim 30$, the average PopIII SMD with scatter maintains a roughly 50% increase over the no-scatter

case. This increase is due to halos drawing low random R values for Equation (12), resulting in halo critical masses lower than the global mean value and earlier star formation than without scatter. The average PopII SMD with scatter is also increased by a factor ~two at the highest redshifts shown, before tapering off and coming into agreement with the no-scatter SMD at the percent level by $z = 15$. PopIII star formation relies solely on a halo overcoming $M_{\rm crit}$, and halos are much more likely to randomly draw a low enough R value to cause earlier star formation than they are to consistently draw high R values that keep $M_{\rm crit,halo} > M_{\rm crit}$. We therefore see a consistent increase in the PopIII SMD that is not strongly reflected by the PopII SMD since it does not depend as directly on $M_{\rm crit}$.

4.3. Baryon–DM Streaming

In Figure 3, we present PopII and PopIII SFRDs and their corresponding $M_{\rm crit}$ values for global streaming velocities of 0–$3\sigma_{\rm vbc}$ (0–90 km s^{-1}). Recall that the velocities stated are those at recombination, which fall off with decreasing redshift. We also show the average SFRD determined by using many global streaming velocities ranging from 0 to $3\sigma_{\rm vbc}$ and weighting each by the probability of the $v_{\rm bc}$ value used. The
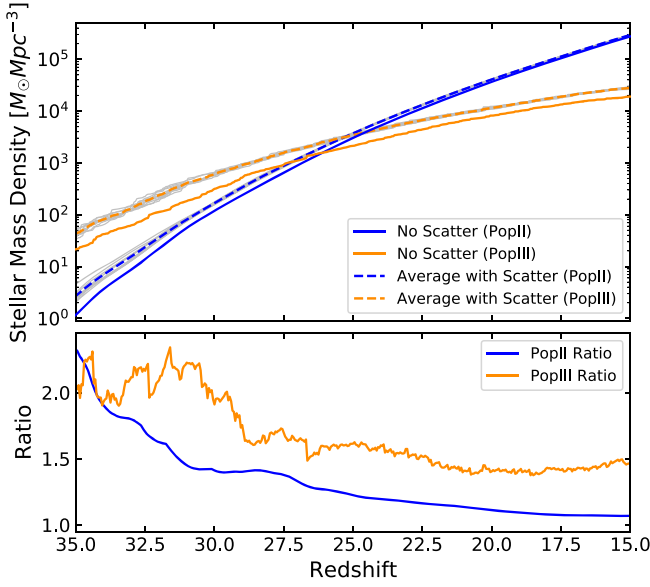
Figure 2. The impact of a critical mass scatter on the results of our fiducial model. Top: the evolution of the SMD over time. The fiducial PopII (blue) and PopIII (orange) SMDs without scatter are shown by the solid lines. The densities for the sample of 10 runs including $M_{\rm crit}$ scatter are plotted in gray, and the averages of these 10 runs for both stellar populations are shown by the corresponding dashed lines. Bottom: ratio of the average SMD including $M_{\rm crit}$ scatter to the fiducial model SMD for each stellar population.

probabilities are determined from the Maxwell–Boltzmann distribution of $v_{\rm bc}$ values found at recombination (Tseliakhovich & Hirata 2010; Tseliakhovich et al. 2011; Fialkov et al. 2012), and these weighted averages are shown by the dashed purple curves in the top and middle panels of Figure 3 for the PopII and PopIII SFRDs, respectively.

We see from the top two panels of Figure 3 that the SFRDs of both stellar populations are increasingly suppressed with faster streaming velocities. This is because higher $v_{\rm bc}$ values increase $M_{\rm crit}$, which delays any PopIII and subsequent PopII star formation. This effect is greater for PopIII since it is directly governed by $M_{\rm crit}$, whereas PopII star formation begins after $t_{\rm delay}$ and depends on the gas mass of the host halo thereafter. The weighted average SFRDs each agree with those of the fiducial $1\sigma_{\rm vbc}$ case to within 50% at $z < 35$, indicating that our fiducial treatment is a reasonable representation of the global streaming velocity. We note that the true baryon–DM streaming velocity varies over spatial distances of a few megaparsecs, a detail that we plan to incorporate into future work.

4.4. Additional Parameter Variations

In this subsection, we explore the effect of various parameter value choices on the resulting SFRDs. To show the impact of our fiducial choices for the PopII SFE and PopIII formation mass, we vary the values of $f_{\rm II}$ and $M_{\rm III,new}$ and plot the resulting SFRDs in the top row of Figure 4. The top left panel shows the SFRDs for four realizations of our semianalytic framework with PopII SFEs ranging from $f_{\rm II} = 0.00125$–0.01. From here we see that the SFRD response is less than linearly proportional to changes in $f_{\rm II}$. Each PopII SFRD shown falls within a factor of four to one another at $z \lesssim 22$, despite the value of $f_{\rm II}$ varying by a factor of eight. Any changes in the PopIII SFRDs ($z \lesssim 30$) are only caused by differences in the PopII SFRDs altering the LW background intensity and thus
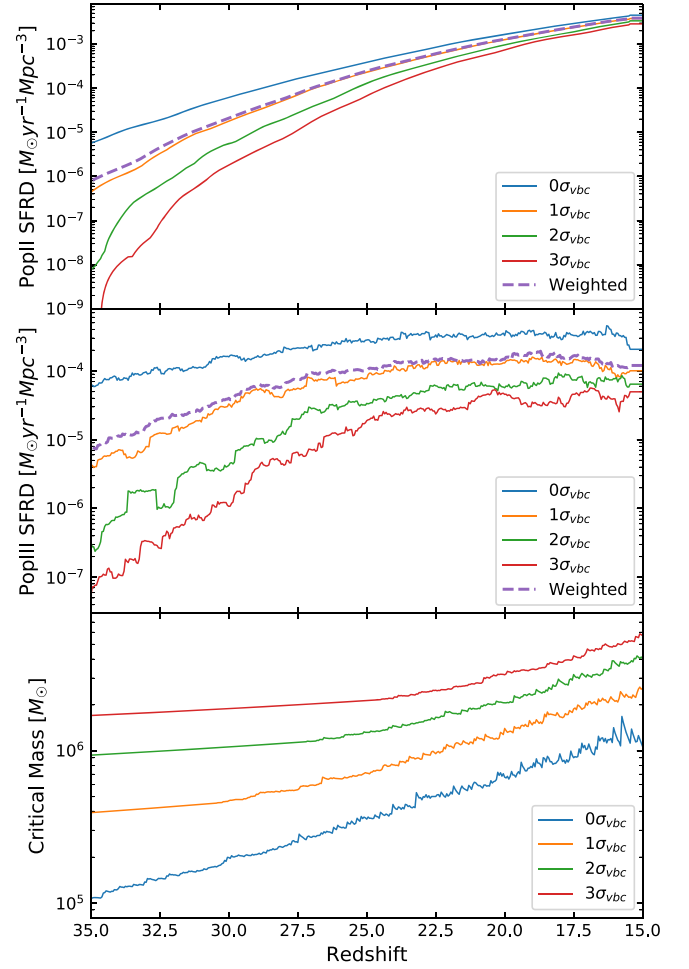

Figure 3. The impact of the relative baryon–DM streaming velocity on the global SFRD and critical mass. Top: PopII SFRDs for four models with global streaming velocities of $0\sigma_{\rm vbc} = 0$ km s^{-1} (blue), $1\sigma_{\rm vbc} = 30$ km s^{-1} (orange), $2\sigma_{\rm vbc} = 60$ km s^{-1} (green), and $3\sigma_{\rm vbc} = 90$ km s^{-1} (red). The average PopII SFRD is also shown (purple dashed), with each SFRD weighted by the probabilities of the streaming velocity used, which is set by a Maxwell–Boltzmann distribution. Middle: same as the top panel, but for the PopIII SFRDs. Bottom: the value of $M_{\rm crit}$ over time for each of the constant velocity runs. The close agreement between the weighted average SFRDs and those of the $1\sigma_{\rm vbc}$ case justifies our fiducial streaming velocity of 30 km s^{-1}.

$M_{\rm crit}$. In each panel, we show the redshift at which the PopII SFRD first surpasses the PopIII one by the corresponding vertical black lines. We see that higher $f_{\rm II}$ values cause the PopII SFRD to first dominate over the PopIII SFRD at earlier times, ranging from $z \approx 27$ for $0.5f_{\rm II}$ to $z \approx 32$ for $4f_{\rm II}$.

Looking to the top right panel of Figure 4, we see the SFRDs for three realizations with varying PopIII formation mass values ranging from $M_{\rm III,new} = 100$ to $800\ M_\odot$, as well as a realization with a constant PopIII SFE of $f_{\rm III} = 0.001$, which instantly converts a fraction $f_{\rm III}$ of a given halo's gas mass into PopIII stellar mass. The PopIII SFRDs with constant stellar mass each fall within a factor of five to one another at $z \lesssim 30$ despite $M_{\rm III,new}$ changing by a factor of eight, meaning that we again find a less than linearly proportional response to varying $M_{\rm III,new}$. Using $f_{\rm III}$ instead gives slightly steeper growth in the PopIII SFRD, but it still falls within a factor of four to the fiducial model throughout the redshifts shown. Since the stellar mass formed in this realization is dependent on halo gas mass, the SFRD more strongly reflects halo mass growth over time. As with $f_{\rm II}$, higher PopIII SFRDs experience increased LW
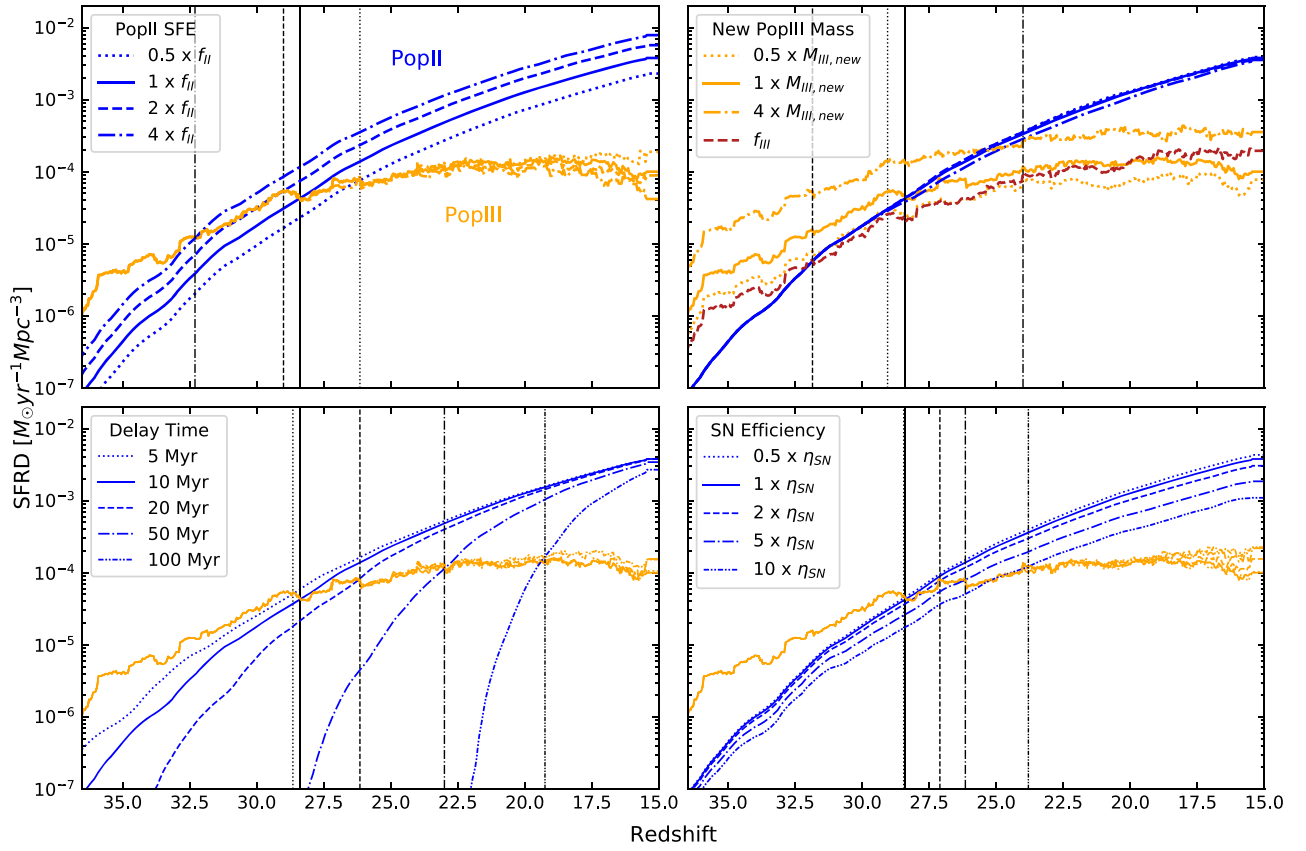
Figure 4. The effect of varying key model parameters on the global PopII (blue) and PopIII (orange) SFRDs. Top left: the impact of varying the PopII SFE on the global SFRD evolution. We vary our fiducial SFE (solid) by multiplying f_{II} by factors of 0.5 (dotted), two (dashed), and four (dotted–dashed). The redshift at which the PopII SFRD first dominates over the PopIII SFRD in each of these simulations is identified by the corresponding vertical black lines in all panels. Top right: similarly, the SFRD impact of varying the PopIII formation mass, $M_{\mathrm{III,new}}$. We multiply our fiducial $M_{\mathrm{III,new}}$ value by factors of 0.5 (dotted) and four (dotted–dashed), and also include the SFRDs resulting from a constant PopIII SFE of $f_{\mathrm{III}} = 0.001$ (dashed dark orange, for clarity). Bottom left: SFRDs for five different values of t_{delay}: 5 Myr (dotted), 10 Myr (solid, fiducial), 20 Myr (dashed), 50 Myr (dotted–dashed), and 100 Myr (dot-dotted–dashed). Bottom right: SFRDs for different SN gas ejection efficiencies: $0.5\eta_{\mathrm{SN}}$ (dotted), η_{SN} (solid, fiducial), $2\eta_{\mathrm{SN}}$ (dashed), $5\eta_{\mathrm{SN}}$ (dotted–dashed), and $10\eta_{\mathrm{SN}}$ (dot-dotted–dashed).

feedback, which boosts M_{crit} and suppresses further star formation. The PopII SFRDs, however, are virtually unchanged by the varying PopIII star formation prescriptions since enriched star formation is mainly governed by the onset of PopIII star formation and t_{delay}.

The t_{delay} parameter represents the delay between PopIII and metal-enriched star formation resulting from feedback associated with star formation and SN winds. To show the impact of this, we vary our fiducial delay time and present the resulting global SFRDs in the bottom left panel of Figure 4. Here we see the SFRDs of five different time delays ranging from 5 to 100 Myr. Unsurprisingly, changes in t_{delay} mostly affect the timing of the initial PopII star formation event. Regardless of the length of the delay, however, enriched star formation quickly overtakes the PopIII SFRD afterwards and gives similar final PopII SFRD values, all agreeing to within 75% at $z = 15$.

To show the effect of the SN ejection efficiency, we vary the fiducial value of η_{SN} in our model and present the global SFRDs in the bottom right panel of Figure 4. Here we see that η_{SN} mostly affects the PopII SFRD at late times, with lower efficiencies yielding higher PopII SFRDs overall. At redshift 15, the $0.5\eta_{\mathrm{SN}}$ case is a factor ∼five higher than the $10\eta_{\mathrm{SN}}$ case. The effect of SN feedback increases with time, partially due to the redshift dependence of v_{esc} in Equation (11) causing more gas to escape over cosmic time.

## 5. Results. II. Impact of Enriched Star Formation and DM Halo Models

In this section, we address the SFRD changes that result from alternative methods for determining the DM halo mass evolution and enriched star formation. We present a direct comparison of the SFRDs resulting from MC merger trees and smooth accretion models of DM halo evolution (as in Furlanetto et al. 2017). We also compare the results of our fiducial enriched star formation prescription (Equations (6) and (7)) to those of a simpler instantaneous model of star formation (e.g., Sun & Furlanetto 2016; Magg et al. 2018; Park et al. 2019; Magg et al. 2022). For completeness, we also include an analytic approach reliant on halo mass function integration to estimate the SFRD (e.g., Visbal et al. 2015b; Mashian et al. 2016; Muñoz et al. 2022; Muñoz 2023).

5.1. Descriptions of Alternative Models

Starting with our smooth accretion model of DM halo evolution, we adopt the abundance matching model described in Furlanetto et al. (2017),

$$\int_{m_1}^{\infty} n_{\mathrm{h}}(m|z_1) \, dm = \int_{m_2}^{\infty} n_{\mathrm{h}}(m|z_2) \, dm, \qquad (13)$$

where $n_{\mathrm{h}}(m|z_i)$ is the number density, n_{h}, of halos with masses $\geqslant m$ at redshift z_i, as determined by the Sheth–Tormen halo
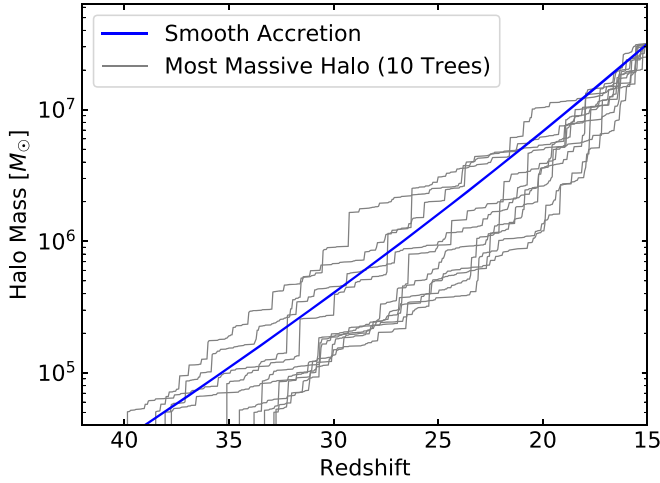
Figure 5. Comparison of mass growth histories for DM halos with a final masses of $\log_{10}(M_{halo}/M_\odot) = 7.5$ at $z = 15$. We show both the MC EPS approach implemented in our fiducial model (gray curves) as well as the smooth accretion method (blue curve) from Furlanetto et al. (2017), each described in detail in Sections 3 and 5, respectively.

mass function (Sheth & Tormen 1999). For a given starting mass m_1 at redshift z_1, we determine the halo mass growth history for a constant n_h by solving for m_2 at each subsequent time step (see Yamaguchi et al. 2023, for a recent example).

Figure 5 shows an example smooth accretion halo mass growth track along with a sampling of MC merger trees with the same final halo mass. While the smooth accretion model follows a constant cosmic number density through time for each halo mass, MC merger trees initialize n_h at $z = 15$ and determine the merger history for a given halo through EPS formalism. The two models produce halo mass evolution tracks that differ on average by a factor ~two at $z \lesssim 35$ due to this discrepancy between Sheth–Tormen and EPS formalism. We note, however, that this discrepancy in the halo mass growth between models is outweighed by the uncertainties in other high-redshift astrophysical parameters implemented here, and thus represents a viable comparison to our fiducial model. We intend to explore alternative DM halo evolution models in future work.

For the "instantaneous" star formation prescription, we compare the SFRDs of our fiducial model with those determining enriched star formation via,

$$M_{*,II} = f_{II,\ i} M_{gas,new}. \tag{14}$$

Here, $M_{*,II}$ is the newly formed PopII stellar mass, $f_{II,\ i}$ is the instantaneous PopII SFE, and $M_{gas,new}$ is the gas mass that has accreted into the halo over the last time step. This method uses a fraction, $f_{II,\ i}$, of the gas mass accreting onto the halo at a given time step to form PopII stellar mass within it instantly. This means that if the halo already has PopII stars, it will not form any more PopII stellar mass until a halo with no prior enriched star formation merges with it and introduces new gas. In the case of two halos with previous PopII star formation merging, no new stellar mass is formed. We include this method into our comparison as it is implemented by semianalytic models throughout the literature in various forms that resemble Equation (14), using an SFE and gas mass to introduce new stellar mass instantly (e.g., Sun & Furlanetto 2016; Magg et al. 2018; Park et al. 2019; Magg et al.

2022). For the rest of this paper, we refer to this PopII star formation prescription as the "instantaneous" method.

For completeness, we also consider the analytic model detailed in Visbal et al. (2015a) to compare with the results of our semianalytic framework. This approach determines the SFRD by integrating the Sheth–Tormen halo mass function, dn/dM, at each time step (also see Mashian et al. 2016; Muñoz et al. 2022; Muñoz 2023, for other examples of this method). Halo mass ranges are defined for both PopII and PopIII such that the cosmic mass fraction collapsed into DM halos, F_{coll}, can be determined for stellar population i via,

$$F_{coll,i}(z) = \frac{1}{\Omega_m \rho_c} \int_{M_{l,i}}^{M_{u,i}} M \frac{dn}{dM}(z)\ dM. \tag{15}$$

Here, Ω_m is the cosmological density parameter for matter and ρ_c is the critical density. In this work, we determine F_{coll} at each time step by integrating the halo mass function from M_{crit}–$2.5\ M_{crit}$ for PopIII, and from $2.5\ M_{crit}$–$10^9\ M_\odot$ for PopII. The time derivatives for both stellar populations, $(dF_{coll}/dt)_i$, are then calculated analytically at each step and are multiplied by $\rho_b f_{II}$ and $\Omega_m \rho_c M_{III,new}$ to give the PopII and PopIII SFRDs, respectively. To match the semianalytic SFRD values more closely, we double the fiducial value of both the PopII SFE and the new PopIII stellar mass in this analytic integration model, i.e., $f_{II} = 0.005$ and $M_{III,new} = 400\ M_\odot$. We also note that we smooth the value of $F_{coll,i}$ over the previous 10 time steps ($\Delta z = 0.5$) to avoid numerical feedback effects when determining its derivative.

5.2. Comparison of Methods

Figure 6 shows the global SFRDs by stellar population for various combinations of DM halo model and star formation prescription, as well as the SFRDs of the fully analytic approach. A key takeaway of Figure 6 is that the merger trees and smooth accretion models for DM halo evolution give similar PopII SFRDs. For a given PopII star formation prescription, instantaneous or via ordinary differential equations (ODEs), the PopII SFRDs of both DM halo models agree to within a factor of two over the redshifts shown.

We also find that the fiducial ODEs for enriched star formation yield steeper PopII SFRD growth than the instantaneous treatment. Calculating the total change in PopII SFRD over the change in time shown in Figure 6 (i.e., $\delta\rho_{*,II}/\delta t$), the slopes given by the ODE prescription are steeper than those of the instantaneous prescription by over a factor of two, given the same DM halo model. In our fiducial prescription, an isolated halo will form stars at a continually decreasing rate, whereas the instantaneous model requires fresh infalling gas, hence the shallower growth of the instantaneous PopII SFRDs.

Looking to the right panel of Figure 6, we find that the PopIII SFRDs of the merger trees have similar qualitative behavior to the smooth accretion SFRDs, but are roughly double their value over the entire redshift range shown. This is a consequence of the discrepancy in halo number densities between Sheth–Tormen and EPS formalism as described in Section 5.1, causing the smooth accretion models to underestimate the PopIII SFRDs by a factor ~two. We verified this by determining the halo mass function given by our EPS merger trees at each redshift then calculating its ratio with
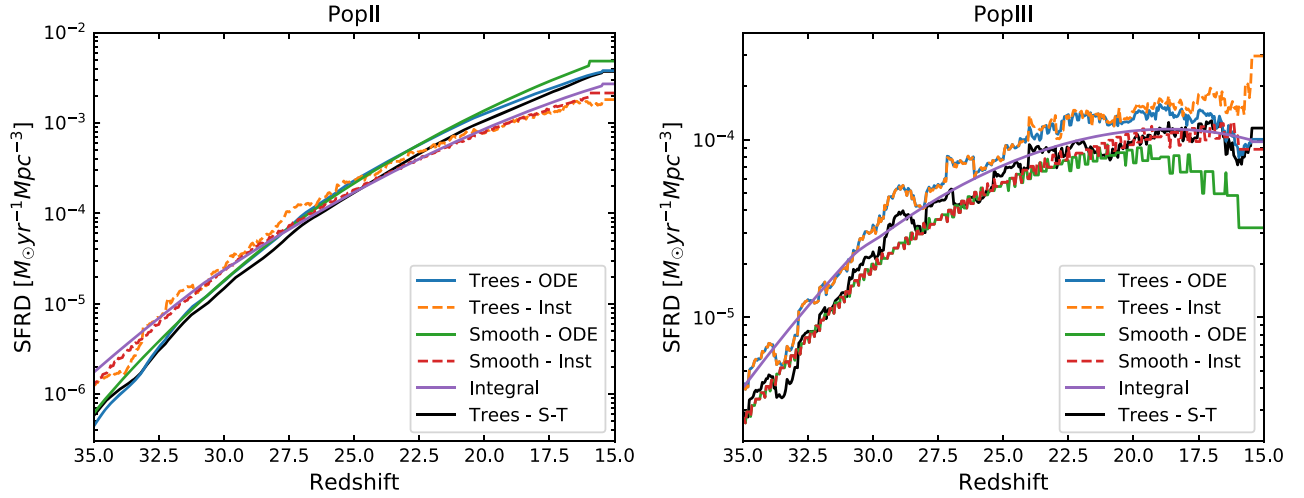
Figure 6. Time-evolution of the global PopII (left) and PopIII (right) SFRDs for different combinations of the methods used for determining the halo merger history and for determining PopII star formation. Models utilizing the EPS merger-tree method are denoted by "Trees" in the legend, and those utilizing the smooth accretion method for halo mass growth (Equation (13)) are labeled "Smooth." Models that use the fiducial set of ODEs for PopII star formation (Equations (6) and (7)) are labeled as "ODE," and those using the Instantaneous method (Equation (14)) are denoted by "Inst" in the legend. Also shown is the fully analytic Integral method (purple), as described in Section 5.1 with a PopII SFE of $f_{II} = 0.005$ and a new PopIII stellar mass of $M_{III,new} = 400\ M_\odot$. Finally, the black "Trees–S–T" curve uses the fiducial ODE PopII star formation method and EPS merger trees for the DM halo evolution, but the halo mass bin number densities, n_i, are weighted to match the Sheth–Tormen halo mass function at each redshift step, as is the case for the smooth accretion models. As discussed in the main text, we find that the smooth accretion gives similar results to the full merger-tree models. Additionally, we find that instantaneous PopII SFRDs change less rapidly with redshift than our fiducial ODE-based prescription.

respect to the Sheth–Tormen halo mass function. We then used these ratio values to weight the SFRs of each individual halo before calculating the SFRD, effectively constraining the halo number densities of each mass bin to match the Sheth–Tormen halo mass function throughout the simulation. The resulting PopIII SFRD in Figure 6 (black) agrees with those of the smooth accretion model to within 15% between $z = 20$ and 35. At lower redshifts the "Smooth–ODE" curve decreases due to its higher PopII SFRD and LW background (discussed further in Section 5.3), and the Sheth–Tormen curve approaches the fiducial SFRD values as the weighting ratios approach unity at $z = 15$.

Looking to the SFRDs determined by analytic integration in Figure 6, we see overall reasonable agreement with the SFRDs of the semianalytic models. In fact, when compared to the fiducial SFRDs, the analytic values agree to within a factor of four and to within ∼65% over the redshifts shown for PopII and PopIII, respectively. The integral PopII SFRD shows better agreement with the instantaneous star formation models, falling within a factor of two and to within 40% over the plotted redshifts for the merger trees and smooth accretion models, respectively. This agreement, however, is a result of tuning the star formation in the analytic integration model to match the results of our semianalytic model. We used a PopII SFE and new PopIII stellar mass that were each twice their fiducial value, and set the boundary between PopIII and PopII star formation to be 2.5 $M_{crit}(z)$. Variations of these parameter values can alter the resulting SFRDs by factors of a few. So while it is able to give order of magnitude agreement with the SFRDs of our semianalytic framework rapidly, purely analytic models miss out on key astrophysics for early star formation, and so tuning is required to match semianalytic values.

### 5.3. High J_{LW} Limiting Smooth Accretion Models

In Figure 6, we see a clear downturn in the "Smooth–ODE" PopIII SFRD at $z \lesssim 20$ (green, right panel). Although this effect

is also seen in the fiducial PopIII SFRD (blue, same panel), it is much more pronounced for the smooth accretion model than it is for the merger trees. This behavior results from a limitation of the smooth accretion model that we have discovered in cases of high LW background intensity. To illustrate the breakdown that smooth accretion models experience in high J_{LW} environments, we artificially increase the LW background by a factor of 10 and compare the resulting SFRDs for merger trees and smooth accretion halos in Figure 7.

The top panel of Figure 7 shows the PopII and PopIII SFRDs for both MC merger trees and smooth accretion halo models, given an LW background intensity an order of magnitude higher than in our fiducial framework. The bottom panel shows the critical mass of the smooth accretion realization on top of a sample of the smooth accretion halo mass growth tracks used. The green mass tracks depict halos that cross M_{crit} at any single point in the simulation, whereas the dashed purple mass tracks do not ever cross M_{crit}.

With a boosted LW background intensity, the critical mass increases more rapidly than in our fiducial model. At $z \sim 19$, the last smooth accretion track crosses M_{crit}, after which no further PopIII star formation occurs. This suggests that smooth accretion models for DM halo mass evolution break down in high-radiation environments, and are unable to form stars as the growth of M_{crit} outpaces the growth of the halos. This is particularly relevant for M_{crit} models with a z dependence that scales with J_{LW}, as in the Kulkarni et al. (2021) model. MC merger trees, with their stochastic halo mass growth histories, cover a wider range of halo masses at all time steps, making the rapid growth of M_{crit} a nonissue for MC merger-tree models. Thus, the complete termination of PopIII star formation in high LW environments represents a limitation to semianalytic models with smooth halo mass growth determined via cosmic number density abundance matching.
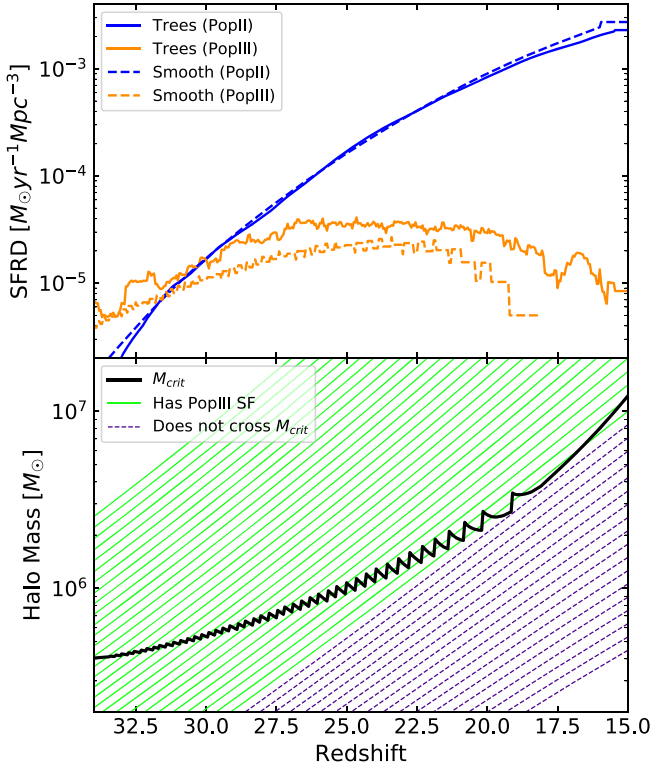
Figure 7. The breakdown of smooth accretion DM halo models in high LW background intensity cases. Top: the PopII (blue) and PopIII (orange) SFRDs for models utilizing MC merger trees (solid) and smooth accretion (dashed) for DM halo mass evolution, and an artificially boosted LW background of 10 $J_{\rm LW}$. Bottom: the critical mass for the smooth accretion model shown in the top panel (thick black) alongside a sample of the halo mass growth tracks used in said model. The mass growth tracks that cross $M_{\rm crit}$ at any point (and therefore form PopIII stellar mass) are shown in green, and those that do not cross $M_{\rm crit}$ at all are shown by the purple dashed lines.

6. Results. III. Realistic Box Volume Simulations

In addition to studying the global star formation history, we also use our model to represent subvolumes of the Universe. We accomplish this by building "boxes" that simulate an ensemble of halos with realistic merger histories for a specified volume. While we cannot model spatial information within these boxes (e.g., the 3D positions of halos), we can compute the variations from region-to-region due to differences in halo number and assembly history. As mentioned above, this is relevant to the large-scale modeling of spatial fluctuations in the high-redshift 21 cm signal which are sourced by fluctuations in star formation. This approach also allows us to determine the extent to which finite simulation boxes (e.g., for hydrodynamical cosmological simulations) systematically underestimate the SFRD due to their lack of density fluctuations on spatial scales larger than the simulation box.

To simulate a finite-volume box, we begin by determining the mean number of halos in each mass bin (which are the same as described in Section 3) at the final redshift of our simulation, $z = 15$. This number is computed using the Sheth–Tormen halo mass function with a power spectrum truncated (i.e., set to zero) at $k_{\rm min} = 2\pi/(\sqrt{3} L_{\rm box})$, corresponding to the longest length scale in the box. This truncation is applied to approximate the impact of boxes with density equal to the cosmic mean as is typically assumed for numerical cosmological simulations. We note that in future work we intend to explore simulating similar boxes with different mean

overdensities, which could then inform the subgrid modeling in large-scale seminumerical models of the 21 cm signal (Visbal et al. 2012; Fialkov et al. 2013; Magg et al. 2022). We sample the number of halos for each mass bin from a Poisson distribution and generate the MC merger trees for each as described in Section 3.1. Our fiducial semianalytic model is then applied to these merger trees assuming an external LW background, $J_{\rm LW}(z)$, computed from our global fiducial model.

We present the results of our finite-volume boxes in Figure 8. Here we show the mean PopII and PopIII SFRDs for 10 boxes of various volumes, and compare them to the SFRDs of our fiducial global model presented above. For boxes smaller than 3 Mpc across, we find that removing power associated with scales larger than the boxes results in a systematic reduction of the PopII SFRD. The PopIII SFRD, however, is less impacted due to it being sourced by smaller halos (with abundance set by the power on smaller scales). From this, we conclude that a 3 Mpc box is sufficiently large to provide an unbiased estimate of the global star formation at $z = 15$–35. One caveat is that this assumes an accurate model of $J_{\rm LW}$ (i.e., from our global fiducial semianalytic simulation) and would not hold if the LW background were computed self-consistently from the finite-volume box. We also note that if the SFRD were to be dominated by more massive halos than in our model, larger-volume boxes would be required for an unbiased SFRD (as likely occurs at lower redshift).

In Figure 8, we also show the scatter of the PopII and PopIII SFRDs for different box volumes. In order to prevent the scatter from depending on our redshift step size, we assign each PopIII star formation burst to a random time between z and $z + \Delta z$, then smooth the results over a 3 Myr period (roughly corresponding to a typical PopIII stellar lifetime). This process effectively allows for star formation to proceed continuously over time instead of at discrete redshift values which bin star formation events into finite time spans, thereby introducing a dependence on the bin size (i.e., Δz) into the error calculations. As expected, the SFRDs increase with higher redshift as halos become increasingly rare. We also note that the fluctuations in PopIII are significantly higher, in large part due to PopIII star formation occurring in instantaneous bursts rather than smoothly across time as is the case for PopII in our model. The scatter is the error one would expect in a single simulation of the given box size. Additionally, these are the levels of scatter one expects in subregions of large-scale seminumerical simulations, as these works typically assume (3 Mpc)³ volume resolution elements corresponding to the scales where $v_{\rm bc}$ does not vary spatially. We find order-unity scatter at $z \sim 35$ and 10% at $z \sim 22.5$ for the PopII SFRD. For the PopIII, we predict order unity at $z \sim 30$ and a value above 20% for all our redshifts ($z > 15$).

In the future, we plan to extend this analysis to overdense/underdense regions to improve the modeling of large-scale 3D spatial fluctuations in star formation history. We note that the size fluctuations shown here represent lower limits because we assume fixed SFEs (i.e., constant $f_{\rm II}$ and $M_{\rm III, new}$). In reality these will vary from halo to halo, and vary over time for a specific halo. In future work, we intend to calibrate the SFEs with hydrodynamical cosmological simulations including star formation and radiative feedback (R. Hazlett et al. 2024, in preparation).
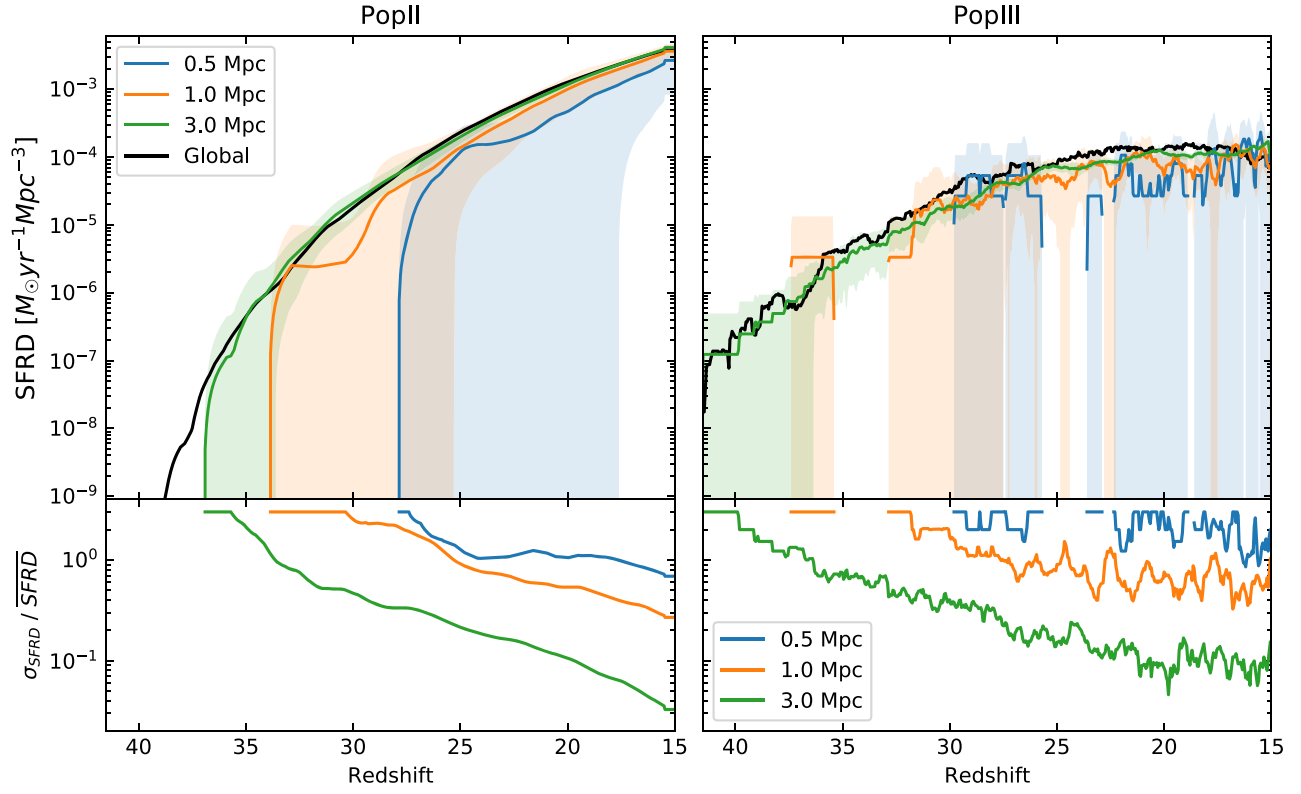
Figure 8. Top panels: the average PopII (left) and PopIII (right) SFRDs for a range of box sizes. Each curve is a 10-realization average and is denoted by the length of one side of the box volume. The shaded regions corresponding to each curve represent the standard deviation of the 10 constituent runs. Also shown are the SFRDs of our fiducial model (black, both panels), which is a globally averaged model and hence, a supposed upper limit for an ever increasing box size. Bottom panels: the error on the mean for each of the PopII (left) and PopIII (right) SFRDs, i.e., the ratio of the standard deviation to the average for each corresponding curve in the top panels.
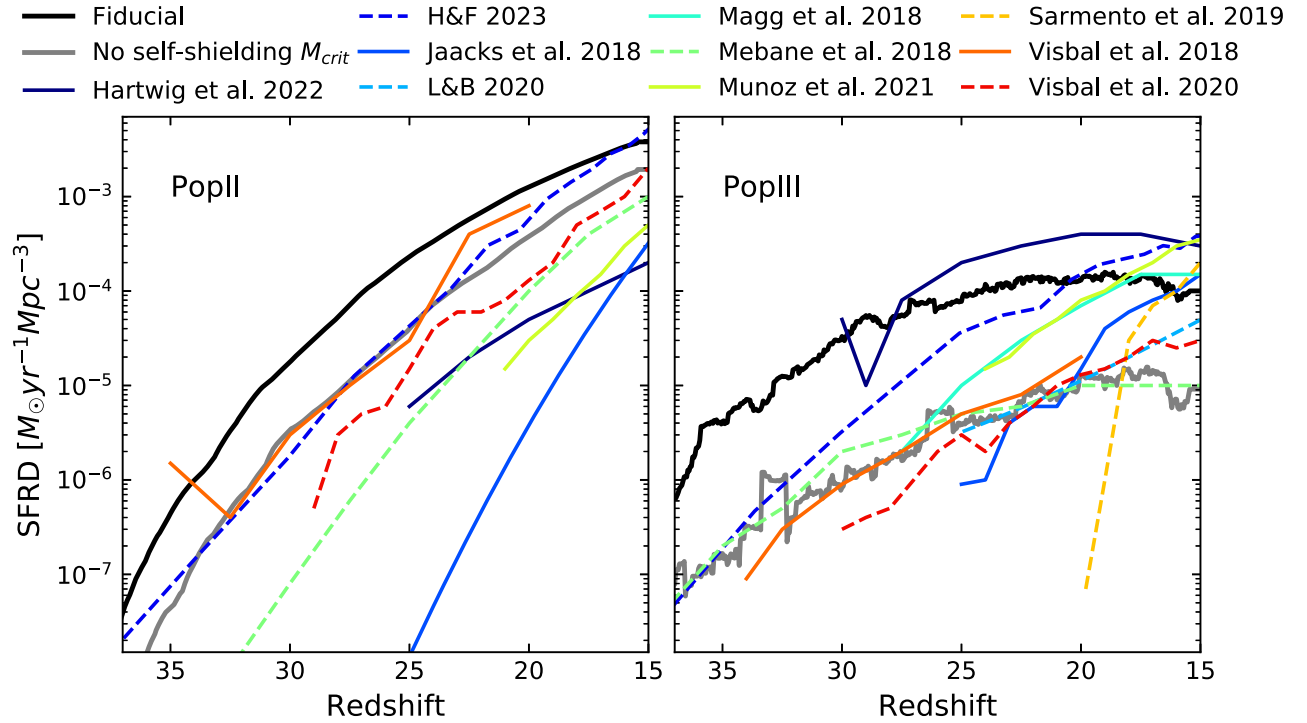
Figure 9. A comparison of the PopII (left) and PopIII (right) SFRDs found in this work with those from the literature. We show our fiducial SFRDs (thick black) and those found using the no self-shielding critical mass model (thick gray, see Figure 1) alongside recently published SFRD histories. These SFRDs alternate between dashed and solid curves for clarity, and are labeled alphabetically by first author surname. Note, for conciseness, Hegde & Furlanetto (2023) and Liu & Bromm (2020) are labeled as "H&F 2023" and "L&B 2020," respectively. We also note that not all referred works include PopII SFRD histories.

7. Star Formation History Comparison with Other Works

We now look to previous works throughout the literature and compare their SFRD histories to those found with our semianalytic framework. Figure 9 shows the PopII and PopIII SFRDs determined by our fiducial model, as well as those using the no self-shielding critical mass (see Figure 1), compared to several recently reported SFRDs from the literature. These SFRDs are the results of a variety of modeling prescriptions including semianalytic simulations (e.g., Magg et al. 2018; Mebane et al. 2018; Visbal et al. 2018; Liu & Bromm 2020; Visbal et al. 2020), cosmological hydrodynamic frameworks (Jaacks et al. 2018; Sarmento et al. 2019), and even a fully analytic model (Muñoz et al. 2022). We note that the majority of the curves shown in Figure 9 are approximations taken from the fiducial SFRD evolution of each reference. This was done by gathering integer redshift SFRD values from plots in each published work, meaning that only broad trends are captured. Exceptions include the PopII SFRD of Jaacks et al. (2018) , which has an assumed functional form, Liu & Bromm (2020) provided a fit for their PopIII SFRD, and the authors of Hegde & Furlanetto (2023) kindly provided us with raw SFRD values resulting from their fiducial framework.

In the right panel of Figure 9, we see that the majority of the PopIII SFRDs shown fall below our fiducial SFRD; however, many of them come into agreement when compared with our no self-shielding M_{crit} realization. The SFRDs reported by Mebane et al. (2018), Visbal et al. (2018), Liu & Bromm (2020), and Visbal et al. (2020) all agree with the no self-shielding M_{crit} PopIII SFRD to within a factor of a few throughout the redshift range shown. In particular, Mebane et al. (2018) and Visbal et al. (2018) are consistent to within a factor of ⩽two across the entire redshift range, despite their respective use of smooth accretion and N-body prescriptions for DM halo evolution. We therefore attribute the general agreement of these semianalytic models with our no self-shielding M_{crit} PopIII SFRD to their use of the same prescription for the critical mass (Equation (5)).

Focusing on a few particular cases in Figure 9, the PopIII SFRD found by Hartwig et al. (2022) shows qualitative agreement with our fiducial model at $z \lesssim 27$, albeit a factor ~three higher. Although they adopt a critical mass model with H_2 self-shielding (Schauer et al. 2021), their J_{LW} is predetermined as a function of redshift, which sets their M_{crit} to five times the threshold found in our self-consistent model at $z = 35$. Once PopIII star formation begins, however, we infer that their high SFE of $f_{III} = 0.38$ per freefall time (calibrated from observations), paired with the limited negative feedback of their analytic $J_{LW}(z)$ prescription, gave this overall higher PopIII SFRD.

Most recently, the semianalytic model presented in Hegde & Furlanetto (2023) has one of the steepest PopIII SFRD evolutions shown in Figure 9. While their critical mass agrees with our fiducial M_{crit} to within a factor of a few throughout, their star formation prescription allows for multiple generations of PopIII stars per halo, a feature that most likely sources such rapid growth.

The PopIII SFRDs resulting from cosmological hydrodynamic simulations in Figure 9 (i.e., Jaacks et al. 2018; Sarmento et al. 2019) are also significantly steeper than those of our semianalytic framework. Since these models mainly cover lower redshifts than what is explored here (each ending at $z \sim 7$), their SFRDs at the redshifts shown in Figure 9 are likely products of the largest halos found in the simulation. Without resolving minihalos at higher redshifts, star formation is confined to the few resolved DM halos that persist at such early times, causing the SFRD to fall off more rapidly. If unresolved minihalos were included, they likely would supplement early star formation and carry the SFRDs at higher redshifts to give more qualitative agreement with our model.

Now looking to the left panel of Figure 9, we see the available corresponding PopII SFRDs which result from a diverse range of star formation prescriptions. On top of this diversity, PopII star formation is frequently affected by other modeling aspects as well (such as the M_{crit} model, f_{II}, t_{delay}, SN feedback, etc.), which makes diagnosing variations between the resulting SFRDs more challenging than with PopIII. For example, Hegde & Furlanetto (2023) determine PopII star formation using our fiducial ODEs adopted from Furlanetto & Mirocha (2022), yet their PopII SFRD grows more consistently than the SFRDs resulting from our framework. This is likely a result of their PopII SFE, which is determined at each time step using a star formation duty cycle, unlike the constant f_{II} value used here. Conversely, the SFRD of Muñoz et al. (2022) is determined via analytic integration of the halo mass function, which, as discussed in Section 5.2, heavily depends on the halo mass ranges over which one integrates and the SFEs used. The PopII SFRDs given by Mebane et al. (2018), Visbal et al. (2018, 2020), and Hartwig et al. (2022) each arise from prescriptions similar to our instantaneous PopII star formation model, but most likely differ in evolution as a result of varying PopII SFEs, varying the halo gas mass used, the inclusion of bursty star formation, and the DM halo model itself.

The SFRDs resulting from this research have extensively shown that one's modeling choices can significantly alter the resulting star formation history. In particular, the right panel of Figure 9 tells us that one must use the improved M_{crit} from Kulkarni et al. (2021) or similar works (e.g., Schauer et al. 2021; Nebrin et al. 2023) that accurately accounts for the effects of H_2 self-shielding and baryon–DM streaming. In general, varying the SFEs of either stellar population can shift their SFRD values up or down with time, and the longer star formation is delayed, the steeper the SFRD growth once it commences.

8. Conclusions and Future Work

In this paper, we presented a new global semianalytic model of the first stars and galaxies at redshifts $z \geqslant 15$. Our model includes complete DM halo merger histories (typically not included in global star formation models at such high redshifts) and is calibrated to the latest numerical simulations (Kulkarni et al. 2021). Here we conclude by summarizing key results from our study and mention directions of future work.

We found that, compared to previous calibrations in the literature, the updated critical halo mass significantly changes the high-redshift SFRDs (mainly due to lower M_{H_2} values as a consequence of molecular hydrogen self-shielding). For instance in our fiducial model, the PopIII SFRD is increased by more than an order of magnitude compared to the no self-shielding critical masses based on the simulations of Machacek et al. (2001), Greif et al. (2011), and Stacy et al. (2012). The PopII SFRD is increased by roughly one order of magnitude at $z = 35$, but falls to a factor of two disagreement by $z = 15$ (see Figure 1).

We also assessed the impact of including the scatter in M_{H_2} due to individual differences in halo merger history and geometry between halos from the simulations of Kulkarni et al. (2021). Figure 2 shows that including this scatter modestly increases the abundance of stars formed. It increased the final PopIII SMD by a factor $\sim$1.5, and the final PopII SMD only increased by $\sim$10% relative to the no-scatter case.

We also studied the effect that DM halo mergers have on star formation history by comparing the SFRDs resulting from MC merger trees to those resulting from smooth accretion based on abundance matching, as described in Furlanetto et al. (2017; Figure 5). For our fiducial astrophysical parameters, we found that the resulting SFRDs (both PopIII and PopII) each agreed to within a factor of two from $z = 18$ to 31 for these DM halo models (see Figure 6). This suggests that the merger history is likely not required to model global SFRDs, provided one does not need an accuracy much greater than a factor of two, but it is required for spatial fluctuations such as those we show in Figure 8. We note, however, that our model does not incorporate changes in astrophysics due to mergers (e.g., an enhanced PopII SFE following mergers), which could occur in more sophisticated star formation models. We also point out that in models with very high J_{LW} (for instance if the SFE was significantly higher than we assume), smooth accretion models have an unphysical shutoff in primordial star formation and a detailed treatment of the merger history may be necessary (see Figure 7).

Additionally, we tested how the global star formation history is affected by our PopII star formation prescription. We compared our fiducial model, based on Equations (6) and (7) (from Furlanetto & Mirocha 2022) to a simpler "instantaneous" method used previously in the literature and found that the instantaneous model leads to a shallower metal-enriched SFRD slope throughout the simulation (see Figure 6). Our fiducial prescription yields steeper PopII SFRDs because it allows halos to continue forming stars in isolation, unlike the instantaneous model which requires infalling gas at each time step (resulting in relatively more late-time formation). The effects of this steeper enriched SFRD manifest in the PopIII SFRD at late times ($z \lesssim 25$) when the increasing LW background intensity sufficiently increases M_{crit} to alter the PopIII star formation history as well.

We also compared our fiducial merger-tree model to a simple integration of the halo mass function based on Visbal et al. (2015b). We found that this analytic calculation closely reproduces the PopII SFRD in the instantaneous prescription, and can reproduce our fiducial enriched SFRD to within a factor $\sim$two. It does a more reasonable job for PopIII, agreeing with our fiducial PopIII SFRD to within a $\sim$65% at the redshifts we explored, but we again note that these SFRDs were the result of tuning the analytic prescription to align with the semianalytic SFRD values more closely.

We showed a comparison of the SFRDs resulting from our semianalytic framework to those from the literature in Figure 9, and found that one's modeling choices can significantly alter the resulting star formation history. In particular, we found that the reduction of M_{crit} due to the effects of H_2 self-shielding and baryon–DM streaming allows for a PopIII SFRD that is about an order of magnitude higher than without the inclusion of such effects. We therefore recommend the use of the critical mass threshold from Kulkarni et al. (2021) or similar works (e.g.,

Schauer et al. 2021; Nebrin et al. 2023) that accurately accounts for the effects of H_2 self-shielding and baryon–DM streaming for predicting global SFRD evolution.

However, since these works investigating the effects of H_2 self-shielding are relatively recent, many uncertainties remain. Although Kulkarni et al. (2021) and Schauer et al. (2021) both utilize hydrodynamical cosmological simulations (ENZO and AREPO, respectively) to probe various redshifts, LW background intensities, and streaming velocities to determine the critical mass for star formation, the thresholds reported by the two works differ by a factor a few. While differences in the simulations used, the parameter spaces probed, and the assumed thresholds for halo cooling/collapse may have contributed to this, exact sources of this discrepancy remain unclear. More recently, Nebrin et al. (2023) published their critical mass model that builds up from halo gas physics to include dependencies on J_{LW} and v_{bc} using (semi-)analytic methods. However, despite hopes that a more analytic approach could shed light on the discrepancy, their resulting M_{crit} seemingly falls between the two models of Kulkarni et al. (2021) and Schauer et al. (2021). We therefore caution the reader to take care when selecting a particular critical mass threshold for future star formation models.

Finally, we used our model to simulate finite-volume boxes each with their own unique set of halos and merger histories (though not including 3D spatial positions). For boxes which are forced to have a density equal to the cosmic mean (as is typically done in nonzoom cosmological numerical simulations), we tested how the lack of power on scales larger the simulation box can impact estimates of the star formation history. We found that a $(3 \text{ Mpc})^3$ box is sufficiently large to provide an unbiased estimate of the global star formation at $z = 15$–35, provided that a reliable external LW background is known (for analytic fits of various LW backgrounds found by our semianalytic model, see Appendix). We also determined the typical scatter in the PopIII/PopII SFRDs as a function of redshift in regions of various volumes that are set to the mean cosmic density.

In future work, we will apply our model to predict large-scale spatial fluctuations in high-redshift star formation, which can then be used to model the cosmological 21 cm signal. We will extend our finite-volume box analysis presented in Section 6 to include variations in star formation as a function of local overdensity and baryon–DM streaming velocity in $(3 \text{ Mpc})^3$ volume elements (as is typically done in other 21 cm predictions; e.g., Visbal et al. 2012; Fialkov et al. 2013). We will then explore ways to emulate our model rapidly, such that it is possible to self-consistently determine the LW background and associated feedback across $\sim$gigaparsec distance scales while also accounting for variations in halo abundance and merger history down to the critical halo mass for forming PopIII stars.

Acknowledgments

Appendix
Fits for the Global LW Background Intensity

Here we detail a sampling of analytic polynomial fits for different LW background intensities resulting from various realizations of our semianalytic model. The fits provided here may be used in finite-volume models to estimate global star formation in the redshift range $z = 15$–35. In the top left panel of Figure 10, we show the $J_{\rm LW}(z)$ resulting from realizations with various $M_{\rm III,new}$ values, and one for the case of no global baryon–DM streaming velocity (solid curves). We show the corresponding fit to each LW background by the identically colored dashed lines. Similarly, the top right panel shows the

$J_{\rm LW}(z)$ for realizations of our semianalytic framework with PopIII star formation determined by an SFE (as described in Section 4.4). The ratio of the model data to the fit of each $J_{\rm LW}(z)$ is then shown in the bottom panels of Figure 10, and we present the coefficients for each polynomial fit in Table 2. For each realization, the coefficients A, B, C, and D describe the LW background intensity in terms of redshift z, via the following function,

$$\log_{10}(J_{\rm LW}(z)) = A(1+z)^3 + B(1+z)^2 + C(1+z) + D. \tag{A1}$$
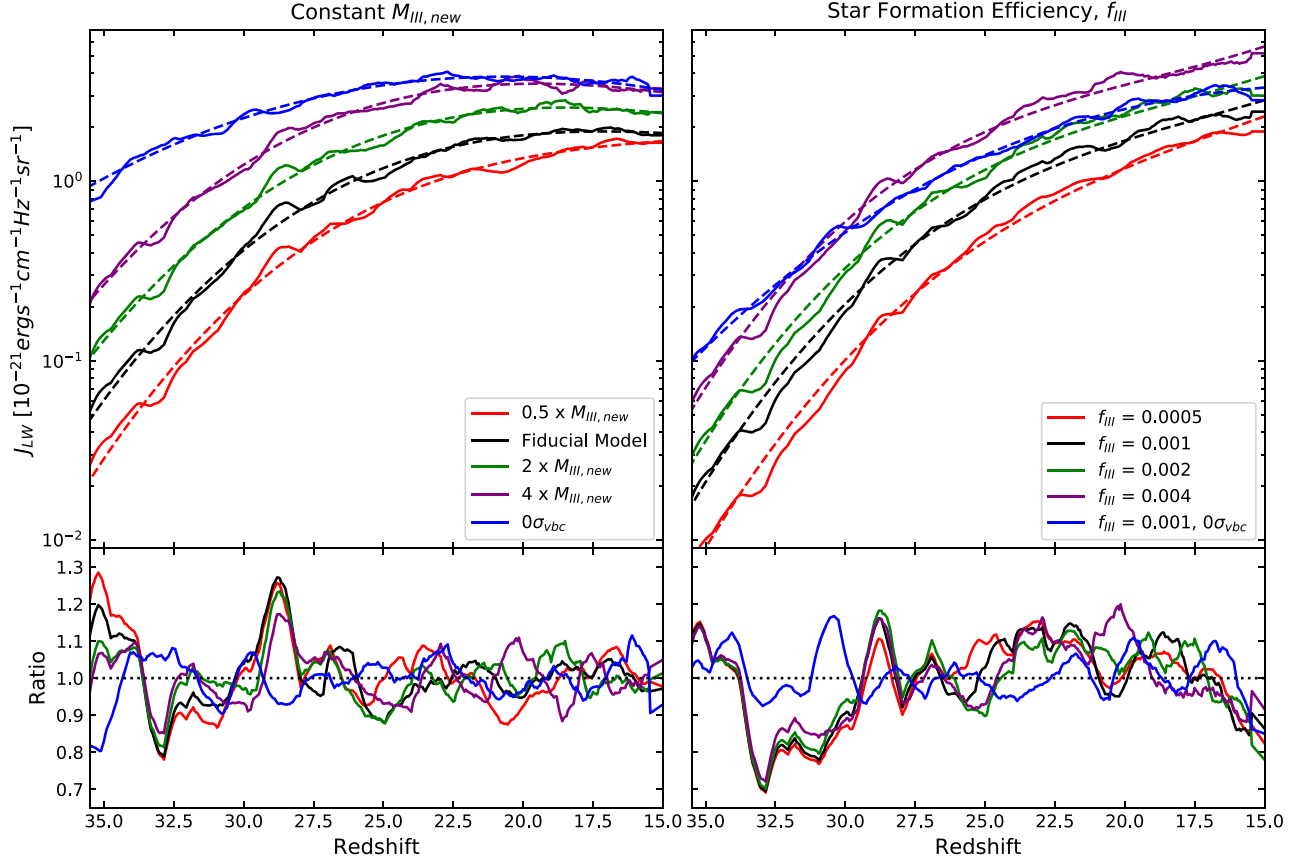
Figure 10. Top left: global LW background intensities for various realizations of our semianalytic framework (solid) and their corresponding analytic fits (dashed). We show the $J_{\rm LW}(z)$ values for our fiducial model (black) alongside those with 0.5 $M_{\rm III,new} = 100\ M_\odot$ (red), 2 $M_{\rm III,new} = 400\ M_\odot$ (green), 4 $M_{\rm III,new} = 800\ M_\odot$ (purple), and for the case with no baryon–DM streaming velocity (blue). Top right: same as top left, but for realizations using a PopIII SFE as described in Section 4.4 (also see Figure 4). Bottom panels: the ratios of each $J_{\rm LW}(z)$ in the upper panels to the values given by their corresponding fits.

Table 2
Polynomial Coefficients Used in Equation (A1) for the $J_{\rm LW}(z)$ Fits Shown in Figure 10

Realization	A	B	C	D
$0.5 \times M_{\rm III,new}$	-1.6246×10^{-4}	7.2219×10^{-3}	-0.11836	0.93553
Fiducial Model	-1.3808×10^{-4}	5.2787×10^{-3}	-5.5111×10^{-2}	0.36564
$2 \times M_{\rm III,new}$	-1.0885×10^{-4}	3.3920×10^{-3}	-8.1113×10^{-3}	8.2743×10^{-2}
$4 \times M_{\rm III,new}$	-1.1377×10^{-4}	4.1009×10^{-3}	-2.4789×10^{-2}	0.30972
$v_{\rm bc} = 0\ {\rm km\ s}^{-1}$	-2.2360×10^{-5}	-9.8214×10^{-4}	7.3987×10^{-2}	-0.33048
$f_{\rm III} = 0.0005$	-1.7990×10^{-4}	8.9799×10^{-3}	-0.20440	2.0708
$f_{\rm III} = 0.001$	-2.0501×10^{-4}	1.0871×10^{-2}	-0.23545	2.2763
$f_{\rm III} = 0.002$	-2.2604×10^{-4}	1.2679×10^{-2}	-0.28003	2.7469
$f_{\rm III} = 0.004$	-2.5241×10^{-4}	1.4942×10^{-2}	-0.33499	3.3205
$f_{\rm III} = 0.001,\ v_{\rm bc} = 0\ {\rm km\ s}^{-1}$	-5.0559×10^{-5}	4.5826×10^{-4}	1.1234×10^{-2}	0.43310

ORCID iDs

Colton R. Feathers ⬤ https://orcid.org/0000-0001-9062-4615
Mihir Kulkarni ⬤ https://orcid.org/0000-0002-9789-6653
Eli Visbal ⬤ https://orcid.org/0000-0002-8365-0337
Ryan Hazlett ⬤ https://orcid.org/0000-0002-1034-7986

References

Abe, M., Yajima, H., Khochfar, S., Dalla Vecchia, C., & Omukai, K. 2021, MNRAS, 508, 3226
Ahn, K., Iliev, I. T., Shapiro, P. R., et al. 2012, ApJL, 756, L16
Ahn, K., Shapiro, P. R., Iliev, I. T., Mellema, G., & Pen, U.-L. 2009, ApJ, 695, 1430
Ahn, K., Xu, H., Norman, M. L., Alvarez, M. A., & Wise, J. H. 2015, ApJ, 802, 8
Barkana, R., & Loeb, A. 2001, PhR, 349, 125
Bond, J. R., Cole, S., Efstathiou, G., & Kaiser, N. 1991, ApJ, 379, 440
Bouché, N., Dekel, A., Genzel, R., et al. 2010, ApJ, 718, 1001
Bouwens, R. J., Illingworth, G. D., Oesch, P. A., et al. 2015, ApJ, 803, 34
Bowman, J. D., Rogers, A. E. E., Monsalve, R. A., Mozdzen, T. J., & Mahesh, N. 2018, Natur, 555, 67
Bromm, V., & Loeb, A. 2007, in AIP Conf. Ser. 937, Supernova 1987A: 20 Years After: Supernovae and Gamma-Ray Bursters, ed. S. Immler, K. Weiler, & R. McCray (Melville, NY: AIP), 532
Burlon, D., Murphy, T., Ghirlanda, G., et al. 2016, MNRAS, 459, 3356
Chiaki, G., Susa, H., & Hirano, S. 2017, MmSAI, 88, 856
Chiaki, G., Yoshida, N., & Kitayama, T. 2013, ApJ, 762, 50
Crosby, B. D., O'Shea, B. W., Smith, B. D., Turk, M. J., & Hahn, O. 2013, ApJ, 773, 108
Davé, R., Finlator, K., & Oppenheimer, B. D. 2012, MNRAS, 421, 98
de Bennassuti, M., Salvadori, S., Schneider, R., Valiante, R., & Omukai, K. 2017, MNRAS, 465, 926
DeBoer, D. R., Parsons, A. R., Aguirre, J. E., et al. 2017, PASP, 129, 045001
Dekel, A., & Mandelker, N. 2014, MNRAS, 444, 2071
Fernandez, R., Bryan, G. L., Haiman, Z., & Li, M. 2014, MNRAS, 439, 3798
Ferreira, E. G. M. 2021, A&ARv, 29, 7
Fialkov, A., & Barkana, R. 2014, MNRAS, 445, 213
Fialkov, A., Barkana, R., Tseliakhovich, D., & Hirata, C. M. 2012, MNRAS, 424, 1335
Fialkov, A., Barkana, R., Visbal, E., Tseliakhovich, D., & Hirata, C. M. 2013, MNRAS, 432, 2909
Finkelstein, S. L., Bagley, M. B., Ferguson, H. C., et al. 2023, ApJL, 946, L13
Frebel, A., & Norris, J. E. 2015, ARA&A, 53, 631
Furlanetto, S. R., & Mirocha, J. 2022, MNRAS, 511, 3895
Furlanetto, S. R., Mirocha, J., Mebane, R. H., & Sun, G. 2017, MNRAS, 472, 1576
Graziani, L., de Bennassuti, M., Schneider, R., Kawata, D., & Salvadori, S. 2017, MNRAS, 469, 1101
Greif, T. H., White, S. D. M., Klessen, R. S., & Springel, V. 2011, ApJ, 736, 147
Griffen, B. F., Dooley, G. A., Ji, A. P., et al. 2018, MNRAS, 474, 443
Haiman, Z., Abel, T., & Rees, M. J. 2000, ApJ, 534, 11
Haiman, Z., & Bryan, G. L. 2006, ApJ, 650, 7
Haiman, Z., & Holder, G. P. 2003, ApJ, 595, 1
Haiman, Z., Rees, M. J., & Loeb, A. 1997, ApJ, 476, 458
Hartwig, T., Bromm, V., Klessen, R. S., & Glover, S. C. O. 2015, MNRAS, 447, 3892
Hartwig, T., Bromm, V., & Loeb, A. 2018a, MNRAS, 479, 2202
Hartwig, T., Yoshida, N., Magg, M., et al. 2018b, MNRAS, 478, 1795
Hartwig, T., Magg, M., Chen, L.-H., et al. 2022, ApJ, 936, 45
Hegde, S., & Furlanetto, S. R. 2023, MNRAS, 525, 428
Hu, W., Barkana, R., & Gruzinov, A. 2000, PhRvL, 85, 1158
Hui, L., Ostriker, J. P., Tremaine, S., & Witten, E. 2017, PhRvD, 95, 043541
Incatasciato, A., Khochfar, S., & Oñorbe, J. 2023, MNRAS, 522, 330
Ishiyama, T., Sudo, K., Yokoi, S., et al. 2016, ApJ, 826, 9
Jaacks, J., Thompson, R., Finkelstein, S. L., & Bromm, V. 2018, MNRAS, 475, 4396
Jeon, M., Pawlik, A. H., Bromm, V., & Milosavljević, M. 2014, MNRAS, 444, 3288
Kaur, H. D., Qin, Y., Mesinger, A., et al. 2022, MNRAS, 513, 5097
Kinugawa, T., Harikane, Y., & Asano, K. 2019, ApJ, 878, 128
Klessen, R. S., & Glover, S. C. O. 2023, ARA&A, 61, 65
Kulkarni, M., Visbal, E., Bryan, G. L., & Li, X. 2022, ApJL, 941, L18
Kulkarni, M., Visbal, E., & Bryan, G. L. 2019, ApJ, 882, 178

Kulkarni, M., Visbal, E., & Bryan, G. L. 2021, ApJ, 917, 40
Labbé, I., van Dokkum, P., Nelson, E., et al. 2023, Natur, 616, 266
Lacey, C., & Cole, S. 1993, MNRAS, 262, 627
Liu, B., & Bromm, V. 2020, MNRAS, 497, 2839
Lupi, A., Haiman, Z., & Volonteri, M. 2021, MNRAS, 503, 5046
Machacek, M. E., Bryan, G. L., & Abel, T. 2001, ApJ, 548, 509
Magg, M., Hartwig, T., Agarwal, B., et al. 2018, MNRAS, 473, 5308
Magg, M., Hartwig, T., Glover, S. C. O., Klessen, R. S., & Whalen, D. J. 2016, MNRAS, 462, 3591
Magg, M., Reis, I., Fialkov, A., et al. 2022, MNRAS, 514, 4433
Mashian, N., Oesch, P. A., & Loeb, A. 2016, MNRAS, 455, 2101
McQuinn, M., & O'Leary, R. M. 2012, ApJ, 760, 3
Mebane, R. H., Mirocha, J., & Furlanetto, S. R. 2018, MNRAS, 479, 4544
Mebane, R. H., Mirocha, J., & Furlanetto, S. R. 2020, MNRAS, 493, 1217
Mellema, G., Koopmans, L. V. E., Abdalla, F. A., et al. 2013, ExA, 36, 235
Mesinger, A., Furlanetto, S., & Cen, R. 2011, MNRAS, 411, 955
Miranda, V., Lidz, A., Heinrich, C. H., & Hu, W. 2017, MNRAS, 467, 4050
Muñoz, J. B. 2023, MNRAS, 523, 2587
Muñoz, J. B., Qin, Y., Mesinger, A., et al. 2022, MNRAS, 511, 3657
Mutch, S. J., Geil, P. M., Poole, G. B., et al. 2016, MNRAS, 462, 250
Naidu, R. P., Oesch, P. A., van Dokkum, P., et al. 2022, ApJL, 940, L14
Nebrin, O., Giri, S. K., & Mellema, G. 2023, MNRAS, 524, 2290
O'Shea, B. W., & Norman, M. L. 2008, ApJ, 673, 14
O'Shea, B. W., Wise, J. H., Xu, H., & Norman, M. L. 2015, ApJL, 807, L12
Park, J., Mesinger, A., Greig, B., & Gillet, N. 2019, MNRAS, 484, 933
Parsons, J., Mas-Ribas, L., Sun, G., et al. 2022, ApJ, 933, 141
Planck Collaboration, Aghanim, N., Akrami, Y., et al. 2020, A&A, 641, A6
Poole, G. B., Angel, P. W., Mutch, S. J., et al. 2016, MNRAS, 459, 3025
Press, W. H., & Schechter, P. 1974, ApJ, 187, 425
Price, D. C., Greenhill, L. J., Fialkov, A., et al. 2018, MNRAS, 478, 4193
Ricotti, M. 2016, MNRAS, 462, 601
Ricotti, M., & Ostriker, J. P. 2004, MNRAS, 352, 547
Samui, S., Srianand, R., & Subramanian, K. 2007, MNRAS, 377, 285
Sarmento, R., Scannapieco, E., & Côté, B. 2019, ApJ, 871, 206
Sassano, F., Schneider, R., Valiante, R., et al. 2021, MNRAS, 506, 613
Schaerer, D. 2002, A&A, 382, 28
Schauer, A. T. P., Glover, S. C. O., Klessen, R. S., & Clark, P. 2021, MNRAS, 507, 1775
Sheth, R. K., & Tormen, G. 1999, MNRAS, 308, 119
Shull, J. M., & Venkatesan, A. 2008, ApJ, 685, 1
Skinner, D., & Wise, J. H. 2020, MNRAS, 492, 4386
Smith, B. D., Regan, J. A., Downes, T. P., et al. 2018, MNRAS, 480, 3762
Smith, B. D., Wise, J. H., O'Shea, B. W., Norman, M. L., & Khochfar, S. 2015, MNRAS, 452, 2822
Somerville, R. S., & Davé, R. 2015, ARA&A, 53, 51
Stacy, A., Bromm, V., & Loeb, A. 2011, ApJL, 730, L1
Stacy, A., Pawlik, A. H., Bromm, V., & Loeb, A. 2012, MNRAS, 421, 894
Sun, G., & Furlanetto, S. R. 2016, MNRAS, 460, 417
Trenti, M., & Stiavelli, M. 2009, ApJ, 694, 879
Trinca, A., Schneider, R., Valiante, R., et al. 2022, MNRAS, 511, 616
Trinca, A., Schneider, R., Valiante, R., et al. 2023, arXiv:2305.04944
Tseliakhovich, D., Barkana, R., & Hirata, C. M. 2011, MNRAS, 418, 906
Tseliakhovich, D., & Hirata, C. 2010, PhRvD, 82, 083520
Valiante, R., Schneider, R., Volonteri, M., & Omukai, K. 2016, MNRAS, 457, 3356
Ventura, E. M., Trinca, A., Schneider, R., et al. 2023, MNRAS, 520, 3609
Vikaeus, A., Zackrisson, E., Schaerer, D., et al. 2022, MNRAS, 512, 3030
Visbal, E., Barkana, R., Fialkov, A., Tseliakhovich, D., & Hirata, C. M. 2012, Natur, 487, 70
Visbal, E., Bryan, G. L., & Haiman, Z. 2017, MNRAS, 469, 1456
Visbal, E., Bryan, G. L., & Haiman, Z. 2020, ApJ, 897, 95
Visbal, E., Haiman, Z., & Bryan, G. L. 2015a, MNRAS, 453, 4456
Visbal, E., Haiman, Z., & Bryan, G. L. 2015b, MNRAS, 450, 2506
Visbal, E., Haiman, Z., & Bryan, G. L. 2018, MNRAS, 475, 5246
Visbal, E., Haiman, Z., Terrazas, B., Bryan, G. L., & Barkana, R. 2014, MNRAS, 445, 107
Whalen, D. J., Fryer, C. L., Holz, D. E., et al. 2013, ApJL, 762, L6
Wise, J. H., Turk, M. J., Norman, M. L., & Abel, T. 2012, ApJ, 745, 50
Wyithe, J. S. B., & Cen, R. 2007, ApJ, 659, 890
Xu, H., Ahn, K., Norman, M. L., Wise, J. H., & O'Shea, B. W. 2016, ApJL, 832, L5
Xu, H., Ahn, K., Wise, J. H., Norman, M. L., & O'Shea, B. W. 2014, ApJ, 791, 110
Xu, H., Wise, J. H., & Norman, M. L. 2013, ApJ, 773, 83
Yamaguchi, N., Furlanetto, S. R., & Trapp, A. C. 2023, MNRAS, 520, 2922

Yung, L. Y. A., Somerville, R. S., Ferguson, H. C., et al. 2022, MNRAS, 515, 5416

Yung, L. Y. A., Somerville, R. S., Finkelstein, S. L., Popping, G., & Davé, R. 2019a, MNRAS, 483, 2983

Yung, L. Y. A., Somerville, R. S., Popping, G., et al. 2019b, MNRAS, 490, 2855

Yung, L. Y. A., Somerville, R. S., Finkelstein, S. L., et al. 2020a, MNRAS, 496, 4574

Yung, L. Y. A., Somerville, R. S., Popping, G., & Finkelstein, S. L. 2020b, MNRAS, 494, 1002

Yung, L. Y. A., Somerville, R. S., Finkelstein, S. L., et al. 2021, MNRAS, 508, 2706